H_∞ Position Control of a 5-MW Offshore Wind Turbine with a Semi-submersible Platform

by

Eduardo Eribert Escobar Aquino

B.A.Sc., Autonomous University of Yucatan, 2015

A THESIS SUBMITTED IN PARTIAL FULFILLMENT OF
THE REQUIREMENTS FOR THE DEGREE OF

MASTER OF APPLIED SCIENCE

in

THE FACULTY OF GRADUATE AND POSTDOCTORAL STUDIES

(Mechanical Engineering)

THE UNIVERSITY OF BRITISH COLUMBIA

(Vancouver)

September 2018

The following individuals certify that they have read, and recommend to the Faculty of Graduate and Postdoctoral Studies for acceptance, the thesis entitled:

H_∞ Position Control of a 5-MW Offshore Wind Turbine with a Semi-submersible Platform

Submitted by Eduardo Eribert Escobar Aquino in partial fulfillment of the requirements for the degree of Master of Applied Science in Mechanical Engineering

Examining Committee

Supervisor	Dr. Ryozo Nagamune
	Mechanical Engineering
Examiner	Professor Jon Mikkelsen
	Mechanical Engineering
Examiner	Dr. Machiel Van der Loos
	Mechanical Engineering

Abstract

Floating offshore wind farms have a potential in capturing wind energy in a cost-effective manner, with advantages of consistent and strong wind over the ocean, and of little noise and visual impacts on humans. However, a wind farm may lose its efficiency due to the aerodynamic wake, which is the turbulence passed from the upstream turbines to the downstream ones. The wake is undesirable because it can not only reduce the total power of the wind farm but also increase the structural loading of the downwind turbines. This wake effect can be mitigated by optimizing the layout of the wind farm in real time according to the wind speed and direction, as well as power output of each turbine.

In this thesis, for a 5 MW floating offshore wind turbine with a semi-submersible platform, an H_∞ state-feedback controller design method is proposed to achieve four objectives simultaneously. The objectives are (1) to relocate its position to a specified target location, (2) to regulate its position there by rejecting wind and wave disturbances, (3) to maintain the harvested power to a target level, and (4) to reduce the angular motion of the floating platform. The target location of the floating wind turbine and the target level of the generated power are assumed to be provided by high-level real-time wind farm optimization. For the controller design, a physics-based control-oriented nonlinear model which was previously developed is adopted. The H_∞ controller design problem is formulated as minimization of the position deviations from the target, of the generator speed fluctuation, and of platform oscillations. The designed controller is validated using the medium-fidelity software Fatigue-Aerodynamic-Structure-Turbulence (FAST). The simulation results demonstrate that the H_∞ state-feedback controller outperforms the linear quadratic regulator with an integrator in various tested scenarios.

The research outcome of this thesis will improve the wind farm efficiency, thereby reducing the wind energy cost and increasing the wind energy utilization.

Lay Summary

The goal of this thesis is to design a control system for repositioning offshore floating wind turbines in real-time. A major deficiency of wind farms is a loss in power production due to aerodynamic coupling between individual turbines. As an upstream machine extracts energy from the wind, downstream machines experience slower wind and produce less electricity. One solution to mitigating this drawback in floating offshore wind farms is to take advantage of the mobility of floating turbines by repositioning their platforms in real-time to minimize aerodynamic coupling. The control system developed in this thesis uses the conventional degrees of freedom of a wind turbine to reposition the floating platform while minimizing undesired angular motions of the structure, since these motions increase fatigue damage and reduce the turbine's lifetime. The major findings of this work show that position control with minimal angular motion is achieved without losses in power output.

Preface

This thesis is an original intellectual product of the author, Eduardo Eribert Escobar Aquino, under the supervision of Dr. Ryozo Nagamune. I performed this work independently and wrote all the manuscript under guidance of Dr. Ryozo Nagamune. All of the work presented henceforth was conducted in the Control Engineering Laboratory at the University of British Columbia.

Table of Contents

List of Tables

List of Figures

List of Acronyms

DPS	Dynamic positioning systems
EKF	Extended Kalman filter
FAST	Fatigue-Aerodynamics-Structure-Turbulence
HAWT	Horizontal-axis wind turbine
IEC	International Electrotechnical Commission
IPC	Individual pitch control
IRENA	International Renewable Energy Agency
LFT	Linear fractional transformation
LMI	Linear matrix inequalities
LQI	Linear quadratic integrator
LTI	Linear time-invariant
MOB	Mobile offshore bases
MPC	Model predictive control
NREL	National Renewable Energy Laboratory

NTM	Normal turbulence model
RMSe	Root-mean-square error
STAM	Sewing thread artificial muscle
SWL	Still water level
TLCD	Tuned liquid column damper
TLP	Tension leg platforms
TMD	Tuned-mass damper
VAWT	Vertical-axis wind turbine
WTS	Wind turbine system

Acknowledgments

I would like to express my most sincere appreciation and gratitude to my supervisor, Dr. Ryozo Nagamune. Your patience, guidance, encouragement, and advice in both my research and my career have been invaluable. I would also like to thank Professor Jon Mikkelsen and Dr. Machiel Van der Loos for their helpful suggestions on improving this thesis.

I wish to acknowledge the CONACYT-Secretaría de Energía-Sustentabilidad Energética for providing the funding which allowed me to pursue this research.

Completing this work would have been all the more difficult were it not for the support and friendship provided by the other members of the Control Engineering Laboratory: Cristopher Cortes, Chenlu Han, Pan Zhao, Mohammadreza Rostam, Sara Hosseinirad, Jihoon Lim, Marcin Mirski, Ran Fan, and Anderson Soares. Further, I am particularly grateful for the assistance given by Ali Cherom Kheirabadi during my master thesis preparation. His willingness to give his time so generously has been very much appreciated.

I feel extremely lucky and grateful to have shared research-related talks and courses with peers from different universities, during my studies: Faisal Al-Qurooni and Ezequiel Hernandez from the University of British Columbia, Akira Doi from the Osaka Institute of Technology, Kamran Shah from Shanghai Jiao Tong University, Shuo Kang from Beijing Jiao Tong University, Tiancheng Zhong from Southeast University and Dr. Ting Yue from Beihang University.

Words cannot express how grateful I am to my parents Eudaldo Escobar and Antonia Aquino for their support and sacrifices. I am also deeply thankful to my beloved fiancée Alejandrina Cabrera for her tremendous encouragement.

Finally, my thanks go to my many friends and family who provided a much-needed break from my studies. Their support, both direct and indirect, helped me to complete my work.

To the almighty God

Chapter 1

Introduction

1.1 Background

1.1.1 Wind Energy

Wind as a source of energy represents a feasible alternative to other energy sources for several reasons. For instance, it is considered an environmental friendly source of energy which is easily accessible. During harvest, there is no production of carbon dioxide or pollutant particles. Furthermore, it does not produce sulfuric acid which contributes to the increase of acid rain. These are notable advantages given the fact that the climate change has increased the mean global temperature by 0.85 °C between 1880 and 2012 [2]. Moreover, humanity have recently experienced the three warmest decades in the last 1400 years from 1983 to 2012 [3]. These radical climatic changes are seen as a consequence of greenhouse gas emissions as echoed by the Intergovernmental Panel on Climate Change. Indeed, this climate change is producing a faster displacement of air particles due to the added energy in the atmosphere by greenhouse gases. This is seen as an opportunity for the wind energy industry because it is currently expected to be able to harness a large amount of energy from the wind by mean of wind turbines [4]. As a result, wind energy is experiencing the best growth rate in recent years among electricity sources. For example, wind energy currently accounts for 5 % of the global generated electricity[1] compared to 3 % in 2014[2] showing a mean annual increment of 55.5 GW of installed capacity[3]. Different strategies are followed to lower the price

[1]The Enerdata Yearbook. https://yearbook.enerdata.net/renewables/wind-solar-share-electricity-production.html. Accessed: 2018-06-15

[2]The Shift Project. http://www.tsp-data-portal.org/Breakdown-of-Electricity-Generation-by-Energy-Source#tspQvChart. Accessed: 2018-06-12

[3]Global Wind Energy Council. http://gwec.net/global-figures/graphs/. Accessed: 2018-08-03

of wind energy in the energy industry.

To reduce the initial financing, wind turbines are clustered within a strategic area and form a wind farm. This contributes to the reduction of costs of the land loan and electrical installation by around 5 to 10 % [5]. Furthermore, feasibility assessment expenditures are dispersed in the project when setting an assemblage of wind turbines. Similarly, other approaches such as new technological advances are implemented to lower wind energy production costs. By way of example, energy technology allows a substantial increment in the cost-effectiveness when wind turbines are located offshore.

1.1.2 Offshore Energy

In order to take advantage of the stronger and steadier winds available far from land, wind turbines are shifted offshore. Since installations of fixed structures are feasible up to 60 meters of depth, floating platforms have been developed to operate in deeper waters. One famous practical application is a 30 MW offshore wind farm launched on October, 2017 in Scotland. The project is called Hywind and is comprised of five wind turbines, each of which can operate at up to 6 MW. This cluster is located 25 km far from the shore of Peterhead and operates at water depths of between 95 and 120 m.

Offshore wind farms offer many advantages over onshore wind farms such as the reduction of power transmission infrastructure and avoidance of disturbing settlers nearby. The cost of transmission infrastructure reduces since offshore wind turbines may be installed closer to populated areas as these tend to be closer to the ocean. Meanwhile, with offshore wind farms, countryside inhabitants are not disturbed by blade shadowing and touristic locations are not subject to visual pollution. Wind farms placed offshore yield other advantages due to its effectiveness. By way of example, offshore wind farms have the capability to provide the additionally needed growth to achieve international sustainable energy protocols such as the Kyoto protocol. The Kyoto Protocol have been established to reduce the dependence on fossil fuels and mitigate the emission of greenhouse gases by encouraging developed nations like the European Union, to subsidize the improvement of green energies [4]. With this in mind, the European Union will experience a boost in installed offshore wind power capacity of up to 40 % by 2020 and 100 % by 2030 [6]. This will lead the offshore energy production to be one of the top sources of renewable energy.

According to an outlook analysis by the International Renewable Energy Agency (IRENA), offshore technology is expected to become the top leader in green energy by 2030 by accomplishing several tasks regarding development of new technology. These are as depicted in Figure 1.1, indicating that the control strategies and layout optimization of offshore systems are a priority and a base to develop a strong and profitable energy technology which benefits humanity. Indeed, offshore energy production cost is now competitive compared with fossil fuels[5]. For instance, offshore energy production cost per kWh was 19.6 USD cents in 2015. A predicted production cost of 12 USD cents can be achieved by 2030 if new technological developments support the reduction of the cost of foundations and improve the efficiency of the energy collector systems.

Nevertheless, offshore wind technology presents challenges such as its reliability and funding expenses. The inconsistent air conditions added to the efficiency of the systems cause an uncertainty in the feasibility of this energy source and therefore, less acceptance by investors. Additionally, the high costs of the initial investment, an estimated of 4,239 USD per kW in 2017 [6], increases the perception of a financial risk. Compounding these challenges is the fact that offshore wind energy is not fully developed technology with little precedent.

1.2 Offshore Wind Turbines

1.2.1 Wind Turbine Configuration

A wind turbine system (WTS) captures the kinetic energy of the wind, converts it to electrical energy, and delivers it to the grid. Some characteristics regarding

[4] United Nations Framework on Climate Change. https://unfccc.int/process/the-kyoto-protocol. Accessed: 2018-06-15

[5] U.S. Energy Information Administration. https://www.eia.gov/outlooks/aeo/assumptions/pdf/table_8.2.pdf. Accessed: 2018-06-13

[6] IRENA. http://resourceirena.irena.org/gateway/dashboard/?topic=3&subTopic=1066. Accessed: 2018-08-03

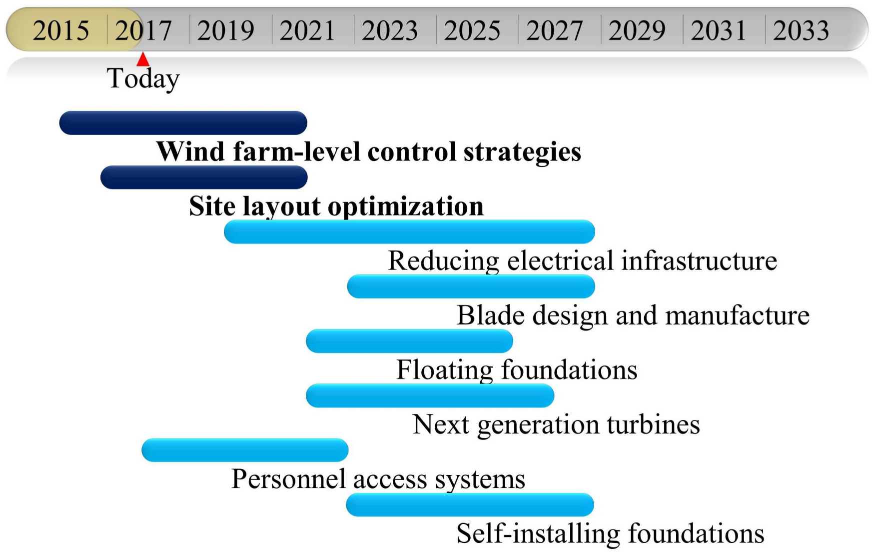

Figure 1.1: The future outlook in research and development for the offshore wind energy industry .

configuration and operation include the direction of the rotation of the turbine's rotor, position of the rotor, and operation flexibility of the generator and the blade mechanism. These features are briefly addressed as follow.

- Dominating the current market, horizontal-axis wind turbines (HAWTs) are more efficient than vertical-axis wind turbines (VAWTs) but also require active control use. On the other hand, VAWTs have less mass and can be used for domestic and small projects.

- In the case of HAWTs, the position of the rotor with respect to the main tower determines whether the wind turbine is upwind (the rotor facing the wind) or downwind (the rotor located on the lee side of the tower).

- Concerning the flexibility of the system, power could be produced using a variable or fixed generator speed. For a variable speed generator, the operation of a WTS can produce more power while requiring utilization of control techniques compared with a fixed speed operation.

- Regarding the blade pitch mechanism, this could also be fixed or variable. A variable pitch mechanism could work independently or in a collective way. These features can enhance the performance of the system as it demands more complex control techniques [7]. These features are used to regulate the power production and reduce induced vibration in the system.

In this thesis, an upwind-HAWT with a variable-collective pitch mechanism is considered. Due to electrical generators technological advances, the utilization of colossal wind turbine structures is more common than in the past allowing to produce more electric power. For HAWTs, their size is related to the swept area of the turbine which proportionally increases with the rated power production. This is expressed as

$$P_{wind} = k_a A = k_a \pi R^2, \tag{1.1}$$

where P_{wind} stands for the aerodynamic power, k_a denotes a constant value, A is the swept area and, R represent the radius of the swept area. Therefore, longer blades and taller towers are needed in order to capture more power from the wind. Nonetheless, mechanical challenges such as vibration can compromise the structure as employed structures increase in size.

1.2.2 Floating Platforms

Floating platforms were initially developed for the oil and gas industry. As easily accessible fossil fuels were depleting, reserves located in deep waters forced the necessity to develop suitable structures to extract fuel from such surroundings. However, the wind energy industry requires different platforms due to some differences. In the oil industry, for example, few stations are placed in the ocean, whereas floating wind farms require platforms for each of their systems. Moreover, wind turbine platforms are much smaller in size compared to those used to extract fossil fuel. As a result, a redesign is needed in order to sustain wind turbines offshore. Among all the different concepts of wind turbine floating platforms, a classification can be made when using the most relevant designs. These are categorized in three groups based on the physical basis and the strategy used to stabilize the entire system. Such classification includes the spar buoy platforms, tension leg platforms (TLP) and semi-submersible platforms.

Spar Buoy

Spar buoy platforms are stabilized using a cylindrical ballasted structure and their displacement is restricted by mooring lines. This design provides high inertial resistance against undesired rotational motions and a considerable draft to prevent abrupt heave displacements. However, due to the weight of the structure, the installation process requires specialized machinery for transport and assembly. An example of a spar-type offshore wind turbine is described in [8], which includes feasibility calculations of the ShortPar turbine for offshore environments. As a result, the ShortPar system was deemed practical at ocean depths up to 150 m.

Tension Leg

TLP are semi-submerged floating structures which are stabilized using stretched mooring lines that fasten the platform to the seabed. This concept allows for lighter and smaller structures compared to spar buoy platforms and it was first presented in [9] for its utilization in the wind energy sector. Nevertheless, the risks of failures while tensioning the mooring lines are high. Another weak point for this platform can be found in its buoyancy principle. Since the mooring lines are always exposed to tension forces that should understand any anticipated loading case, higher anchor loads are experienced in this offshore floating platform configuration. Consequently, the manufacturing of the mooring lines employed is relatively more expensive than other concepts [10].

Semi-submersible

First documented in [11], the semi-submersible floating platform is motion-restricted by mooring lines. The difference with the spar-buoy concept lies in that this design makes use of dispersed buoyancy by employing multiple columns with heave plates. Thus, it requires heavy and large components; however, the installation process is easier and less risky than those mentioned beforehand. This is the platform employed in this thesis for simulation purposes. The WindFloat foundation, which is presented in [12], is a variation of the floating platform structure used in this thesis.

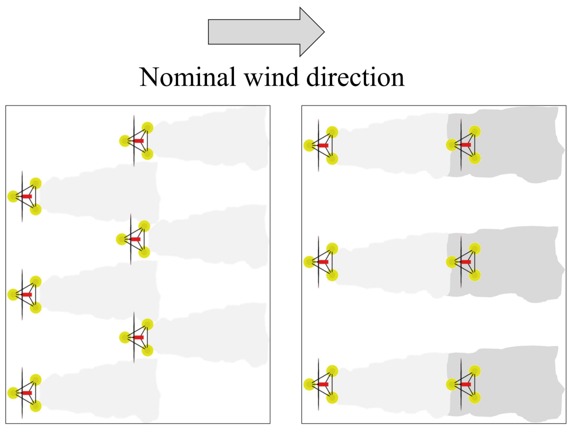

Figure 1.2: Optimal wind farm layout (left) and wake effect representation (right)

1.3 Literature Review

1.3.1 Wake Effect Reduction

The kinetic energy of the air flowing past a WTS is captured by the turbine blades and transferred to the generator, commonly through the rotor shaft connected to a gearbox and then to the generator shaft. The viscous interactions between the air and the blades increase the turbulence intensity of the fluid downstream of the rotor, and also reduces its velocity. In a wind farm, an upstream WTS will generate this slow and turbulent air flow which will then be incident on a downstream WTS. This phenomenon is known as the wake effect and it is depicted in Figure 1.2. A downstream WTS that is located near the upstream WTS cannot generate a sufficient amount of energy from this slow and turbulent source; therefore, WTS are normally placed seven or more rotor diameters apart from each other in the prevailing wind direction in order to decrease the impact of the wake effect. This distance is restricted by the use of land occupied by the wind farm; in such cases, the wake effect cannot be fully avoided. The wake effect diminishes the overall power production of the wind farm, resulting into monetary losses [13]. For instance, a 100 MW wind farm working at 35 % of its capacity results in an annual loss of 602,700 USD [14]. Additionally, [15] reported a drop in power production efficiency of approximately 40 % due to the wake effect. This data came from Horns Rev, a

Table 1.1: Wake effect reduction techniques in the literature

<table>
<tr><td colspan="3">(i) Power derating</td></tr>
<tr><td rowspan="3">(ii) Wake deflection</td><td colspan="2">Yaw-misalignment</td></tr>
<tr><td colspan="2">Tilt-misalignment</td></tr>
<tr><td colspan="2">IPC</td></tr>
<tr><td rowspan="4">(iii) Wind turbine relocation</td><td rowspan="3">Active mechanisms</td><td>DPS</td></tr>
<tr><td>Winch mechanism</td></tr>
<tr><td>STAM</td></tr>
<tr><td colspan="2">Passive technique</td></tr>
</table>

Danish offshore wind farm comprised of an array of eight-by-ten WTSs.

Different approaches for avoiding the wake effect are reported in the literature. In the following paragraphs, three main wake reduction techniques are reviewed. These are power derating, wake deflection and real-time layout relocation, summarized in Table 1.1. We conclude that the repositioning approach, specifically the passive technique, stands out among the others.

Power Derating

The oldest method for mitigating the wake effect is the method of power derating depicted in Figure 1.3. The basic idea here is that reducing the rate of energy extraction from an upstream turbine, which also reduces the overall thrust force exerted on the wind, increases the wind speed that is incident upon a downstream wind turbine [16]. Due to the impact of individual turbine power extraction on the power production on the overall wind farm, any wind farm controller must calculate the optimal power output of each wind turbine within a wind farm [17]. The wind turbine controller developed in this thesis is therefore designed to track any power set-point in addition to the control of other control objectives.

Wake Deflection

Techniques such as yaw-misalignment [18, 19, 20], tilt-misalignment [21] and individual pitch control (IPC) [22] are briefly introduced as part of the wake deflection technique depicted in Figure 1.4. A WTS can make use of its nacelle yaw mechanism to skew the downstream wake to the side, thus reducing the overlap

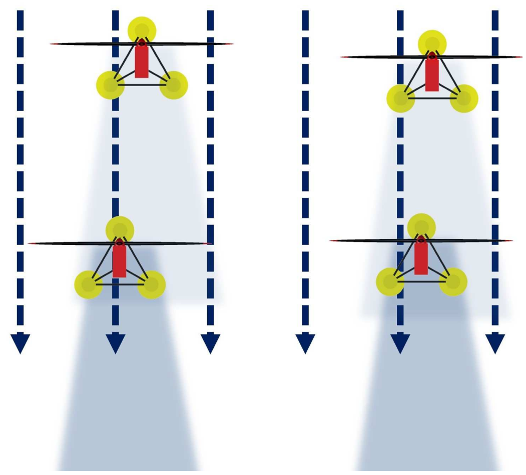

Figure 1.3: Power derating method

area between the wake and a downstream turbine. It is mentioned that the application of this technique showed enhancement of the overall power produced by wind farms and reduction of loads applied to downwind WTSs. However, blade loads did increase, thereby shortening their lifetime. Moreover, its implementation is challenging because of the dependence of the yaw mechanism controller on the wind direction and position of the downstream WTS. Similarly, the tilt-misalignment approach diverts the undesired turbulent air flow, but in the vertical direction. This method is not easily affected by changes in the wind direction; nevertheless, the needed tilting as well as the required turbine spacing to avoid major damages due to the wake effect in a downstream structure make this technique infeasible. In fact, tilting the nacelle brings the blades closer to the main tower which deteriorates the integrity of the structure. Additionally, IPC was shown as an alternative to yaw and tilt misalignment and even when observing notable results at particular cases, loads applied to the blades are significantly raised. In addition to wake deflection, real-time repositioning is considered to avoid the wake effect.

In [23], reliable simulations were conducted by the National Renewable Energy Laboratory (NREL). The simulation framework included two WTSs positioned in a row so that the wake effect can be seen acting on the second model. Simula-

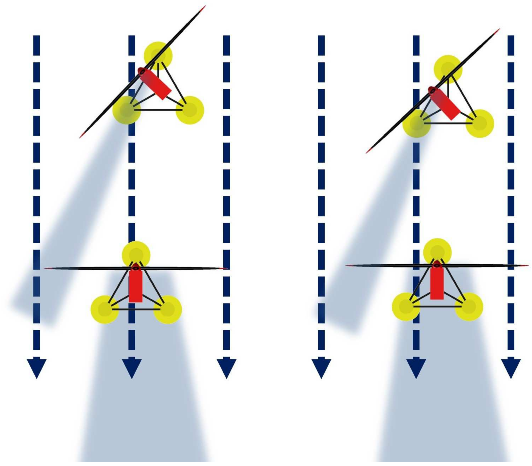

Figure 1.4: Yaw-misalignment technique to deflect the wake in order to avoid downstream WTSs

tions were run under diverse scenarios for the purpose of the performance comparison between wake skewing and WTS relocation regarding power production of the downwind system. Taking as a baseline results without considering any wake avoiding method, power generation improved by 41 % when shifting the downstream turbine in the crosswind direction. Yaw and tilt misalignment only increase the wind farm power generation by 4.6 and 7.6 %, respectively. Furthermore, the simulations displayed that added loads were barely experienced by the downwind turbine once the lateral spacing between models reached one full rotor diameter of difference when using the repositioning method; whilst yaw and tilt misalignment techniques presented higher undesired loads applied to the downstream turbines due to the partial wake overlap. For this reason, active and passive real-time reposition strategies have been developed.

Wind Turbine Relocation

Mobility is an inherent feature in spar buoy and semi-submersible platforms and may be exploited to enhance the overall performance of the wind farm. Examples of actuated approaches found in the literature include: dynamic positioning

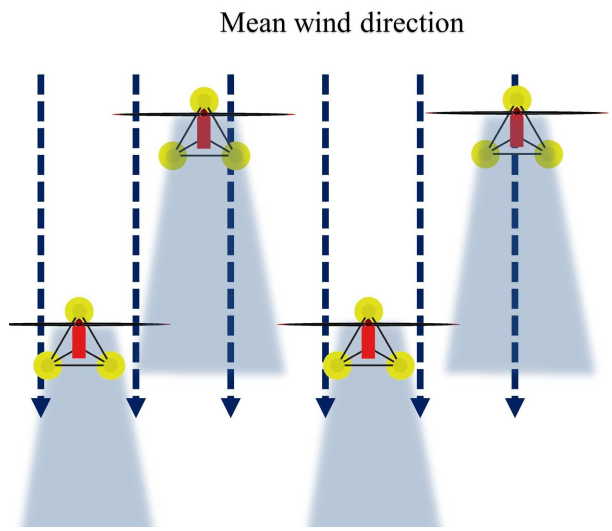

Figure 1.5: Wind turbine relocation employed to reduce the wake effect by optimizing the wind farm position layout

systems (DPS) [24], winch mechanisms [25] and sewing thread artificial muscle (STAM) [26]. An example of wind turbine relocation is depicted in Figure 1.5.

Firstly, DPS actively controls the position of an offshore platform through the utilization of thrusters. It is widely used in diverse deep-sea applications such as oil and gas extraction, drill, mobile offshore bases (MOB) and others. This system provides high precision when tracking and keeping desired positions, and its performance is faster compared to other approaches; moreover, restriction of mooring lines is not needed as this device can operate continuously. Despite the many advantages offered by this method, its application for offshore wind power extraction is infeasible. Different from offshore fossil fuels extraction, wind turbine floating platforms are smaller and greater in number when considering a wind farm; accordingly, multiple DPSs are needed for each structure. Besides, DPSs are not cost-effective because they are required to be powered for tracking and station keeping, and, unlike fossil fuels, wind power extraction is not regular.

Secondly, the winch mechanism concept was presented as an alternative positioning method. The winch device provides one or two extra degrees of freedom depending on the configuration employed. It is set up to adjust the length of a mooring line in order to control the position of a floating WTS. When the desired position has been achieved, the winches stay locked so that the platform keeps steady. In that case, the mechanism does not consume electricity once fixed. However, there are no further reports by the company related to the realization of this concept; so even if the design is functional, its profitability remains uncertain.

Thirdly, the actuator STAM simulates the contraction and relaxation of a muscle by changing the temperature of the composed threads. It was developed as an active method to reduce vibrations in TLPs by adjusting the tension of the mooring lines. Although this mechanism was not designed specifically for the relocation of floating platforms, this could be achieved when this actuator replaces conventional mooring lines for spar buoy and semi-submersible platforms. Similarly to the winch mechanisms, this actuator can regulate the distance between the floating platform and the seabed. Unfortunately, the STAM is still under evaluation; so its cost-effectiveness is not yet known. Further, its feasibility and performance cannot be assured at this point.

The work in [27, 28] presents a viable alternative to passively relocate a floating offshore wind turbine. By taking advantage of the aerodynamic force experienced by the floating wind turbine and the restoring force from the mooring lines, it was demonstrated that it is possible to passively change and keep the position of the floating platform within a defined area in real-time. This movable range depends on two parameters: the average wind speed and the power generation level. According to the authors, there is no need for additional actuators besides blade pitch angle (collective), applied torque generator, and nacelle yaw angle to achieve such a goal. Thrust can be experienced by the floating WTS due to the aerodynamic interaction between the wind and the turbine's rotor, especially on the blades. In fact, the system can be modulated using the collective pitch blade mechanism, which can set the backward or forward displacement of the floating platform. Additionally, the lateral movement is achievable when rotating the nacelle yaw mechanism, generating an angle of attack as if it were a sail. Nonetheless, there is some room for improvements in disturbance rejection.

1.3.2 Angular Motion Reduction

Even when the wake effect is avoided, the offshore environment consists of wind and waves that affect the motion of the turbine and generate additional loads. These additional loads negatively affect the WTS by increasing fatigue damage and reducing its lifetime. This raises the requirement of more costly components, and increases maintenance costs and the probability of failure. Passive structural control techniques, as well as active control schemes, have been applied to offshore wind turbines in order to reduce induced angular motions due to disturbances such as wind and waves. These are briefly reviewed.

Structural control involves the regulation of structural reactions through the generation of forces or the improvement of damping by means of mechanisms or materials. Besides the previously mentioned STAM actuator, some other structural controllers have been presented in the literature, like the tuned-mass damper (TMD) [29] and the tuned liquid column damper (TLCD) [30, 31]. A TMD is a device for structures that passively absorbs energy at a desired frequency. This system can be modeled as a mass-spring-damper where the spring constant and the damping constant can be tuned to match the natural frequency of the wind turbine structure. A TMD mechanism is placed at the top of the nacelle along one direction to reduce either fore-aft or side-side vibrations. Although two devices can be placed orthogonally in order to cover both axes, a more complex wind turbine redesign is necessary to avoid interference between a fore-aft TMD setup and the rotor of the turbine. Furthermore, the installation is not an easy task and requires time and heavy duty equipment, primarily due to the fact that these devices can be very heavy, an average of 20 tonnes of mass. In the same way, TLCDs were developed as another structural control device derived from TMDs. In contrast, the TLCD uses the gravitational restoring force from fluid located in a U-shaped damper. The damping effect depends on the liquid selected and can be tuned to match the natural frequency of the structure in order to counteract resonance. TLCDs are also lighter and easier to install compared to TMDs. Nevertheless, considerable adjustments are still needed in order to connect this device to the WTS. Together with its low bandwidth of actuation, its control algorithms become increasingly complex with each additional direction of damping. Accuracy could not be guaranteed when this method is shifted towards deeper waters, so it is impractical. Hence, some non-invasive approaches were proposed in order to reduce disturbances using control schemes.

Additionally, the regulation of floating platform motions by means of the usage of the blade pitch mechanism to regulate the aerodynamic thrust was reported in the literature. [32] implemented a closed-loop blade pitch control system to reduce the perturbations of a floating offshore wind turbine. The controller consisted of a linear quadratic regulator (LQR) and was designed to reject only wave disturbances. Additionally, contrary blade pitch actuation was employed to reduce platform moments induced by the waves. As a result, a reduction was seen in the motion of the platform as well as the deviation of the power generated and the usage of the blade pitch actuator. Lastly, an extended Kalman filter (EKF) technique was applied to estimate the states and disturbances. One drawback in this study was that the controller was designed based on the dynamic model of an onshore wind turbine. The performance of the controller may be improved if it is based instead on an offshore WTS dynamic model.

Another control strategy was implemented in [33] to reduce the induced wave disturbance effect on the floating platform motions by means of the blade pitch mechanism. Based on the performance of a model simulated in still water without disturbance, a model predictive controller (MPC) optimized the behavior of a wind turbine model within an offshore environment with waves and wind. The disturbed system was forced to follow the state trajectories of the non-disturbed model at each time step. First, a state estimator was used to obtain the response of the perturbed system a few samples in advance. Then, the collected non-linear model is linearized for the present operating point so that the open-loop matrices can be determined. Finally, the blade pitch actuation driven by the MPC is optimized to match this result with the behavior shown by the undisturbed model at the same operating point. Consequently, the same procedure is required periodically as every measurement changes at each sample time. The results showed a decrease in the motion of the floating platform, which translated to load reductions in the mooring lines and fairleads[7] at expense of more blade pitch actuation and higher

[7] A fairlead is a device that guide the mooring lines by restricting its lateral motions.

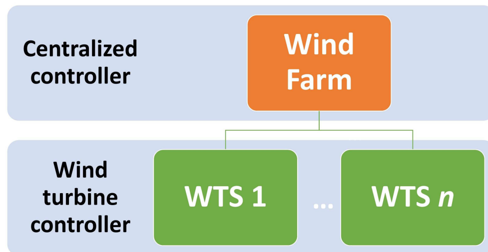

Figure 1.6: Wind farm control scheme hierarchy comprised of a main wind farm control level and multiple wind turbine controllers

loads experienced in the tower. Although the simulation outcome was promising, the high computer processing power demand makes this option infeasible in real life.

Lastly, previous works addressing on-land wind turbines employing the H_∞ norm minimization approach are presented. Such is the case described in [34], where a multi-variable H_∞ controller was designed to reduce loads in a WTS. By means of the blade pitch mechanism, the closed-loop system demonstrated a reduction of tower and blade loads compared with a PI baseline controller. Also, an experimental setup was used in [35] to validate the performance of the H_∞ approach in a practical applications. The H_∞ controller efficiency in terms of load reduction is compared against a classical iterative design approach. Therefore, the H_∞ controller shows significant enhancement in terms of load reduction while reducing the usage of control inputs. This type of controller is extended to floating offshore applications in the current thesis.

1.3.3 Control Scheme Hierarchy

Figure 1.6 displays the control hierarchy for wind farm control. The wind farm controller supervises the overall performance of the n number of wind turbines within the wind farm; its main task is to maximize power production. The wind farm controller therefore specifies the optimal operating point of each turbine in order to maximize the overall power production. In the case of position control, the wind farm controller calculates the ideal position that each turbine should track and maintain in order to minimize the wake effect. This calculation must be performed

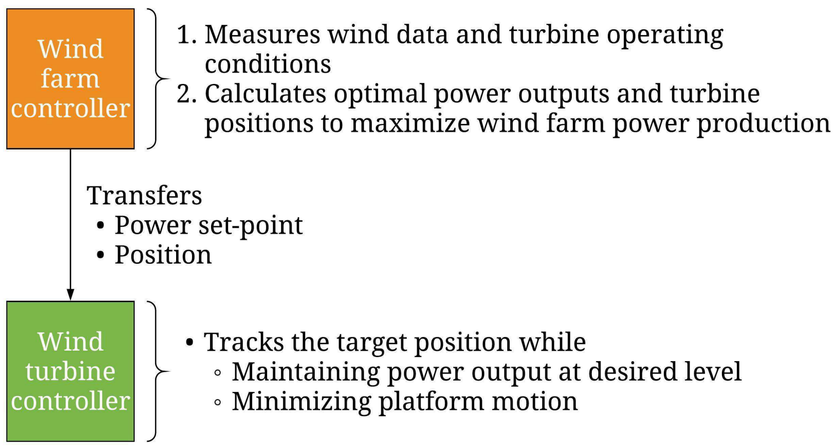

Figure 1.7: Tasks of the control levels of a wind farm and their interaction

periodically based on wind speed and direction. The optimal wind farm layout and turbine positions are then communicated to the individual turbine controllers.

Each wind turbine controller monitors four processes; startup, shutdown, park and power production of the WTS. Regarding the power production task, the operation is usually divided into three different regions depending upon the mean wind speed. The first region is limited to wind speeds that are insufficient for maintaining rotor rotation and power production; the turbine remains parked in this case. The second region is limited to wind speeds that are sufficient for maintaining stable operation of the wind turbine and providing electrical energy to the grid while remaining below the rated wind speed of the turbine.The control objective in this region is to maximize energy production. Finally, the third region is limited to wind speeds above the rated wind speed of the turbine. In this case, the control objective is to maintain the turbine's rated power production while minimizing loads. In addition to these tasks, the wind turbine controller has the task of tracking the set points specified by the wind farm controller. Furthermore, if minimizing platform motion is also included as part of each turbine's control objectives, which is the case in the current work, there exists a trade-off between motion minimization and power production. The interaction of both control levels is depicted in Figure 1.7

1.4 Research Objective

The objective of this thesis is to design a robust position controller for an offshore WTS with a semi-submersible floating platform. This controller relocates and maintains a floating wind turbine at a desired point while minimizing platform motions influenced by perturbations of the waves. At the same time, it attempts to maintain the harvested power at a target level. It is assumed that the desired position and power targets are provided by a wind farm controller, which calculates the optimal layout. Furthermore, the reduction of the angular motions induced by the waves is considered in the robust controller design. This is important for enhancing the lifetime of the wind turbine structure.

1.5 Organization of the Thesis

The presented dissertation is divided into six main chapters, and the first one is this introduction. In Chapter 2, the formulation of the problem to be solved is documented. First, a brief description of the offshore WTS is shown. Furthermore, the objectives of the controller to be designed are set. A review of the mathematical models used in this thesis can be found in Chapter 3. This is comprised of the software FAST employed for simulation purposes as well as a physics-based simplified model utilized for the design of the robust controller. Moreover, the movable range concept is addressed to expand previous knowledge regarding position control. The novel multi-objective robust controller is described in Chapter 4. Subsequently, in Chapter 5 the simulation results are analyzed in order to describe the performance of the closed-loop system employing the proposed robust controller. Three different simulations are included: a comparison against a LQI controller, a tracking process and the response of the robust controller against higher wind and waves perturbations. Finally, the conclusions and potential future works are documented in Chapter 6.

Chapter 2

Problem Formulation

In this chapter, a brief description of the offshore WTS with a semi-submersible platform utilized in this thesis is presented in Section 2.1. The multi-objective controller design problem is formulated in Section 2.2, where the position control, power regulation and the angular velocity reduction are explained.

2.1 Offshore WTS With a Semi-submersible Platform

The wind turbine model used in this thesis is the baseline 5 MW HAWT mounted on a semi-submersible platform which has been designed for control systems research by NREL. This model is very popular in the engineering field as a reference for research because of its accuracy and detailed description.

2.1.1 Description of the NREL 5-MW WTS

The NREL 5 MW baseline wind turbine depicted in Figure 2.1 was first presented in [1] as an alternative to a realistic model used to standardize baseline wind turbine specifications. The model specifications are based on a collection of different real wind turbines rated at 5 MW, such as the REpower and the Multibrid M500 [36], plus calculations based on wind turbine concepts like WindPACT [37], DOWEC [38], and others. The control degrees of freedom of the wind turbine include the collective blade pitch angle, the generator torque and the nacelle yaw angle, displayed in Figure 2.2. The actuators are therefore the driving mechanism for these degrees of freedom. The saturation and rate limits of these degrees of freedom are shown in Table 2.1. The turbine drivetrain is driven by three blades of 61.5 m length. Each blade is able to rotate along its pitch angle independently through a mechanism that operates at a maximum rate of 8 deg/s. The rated rotor

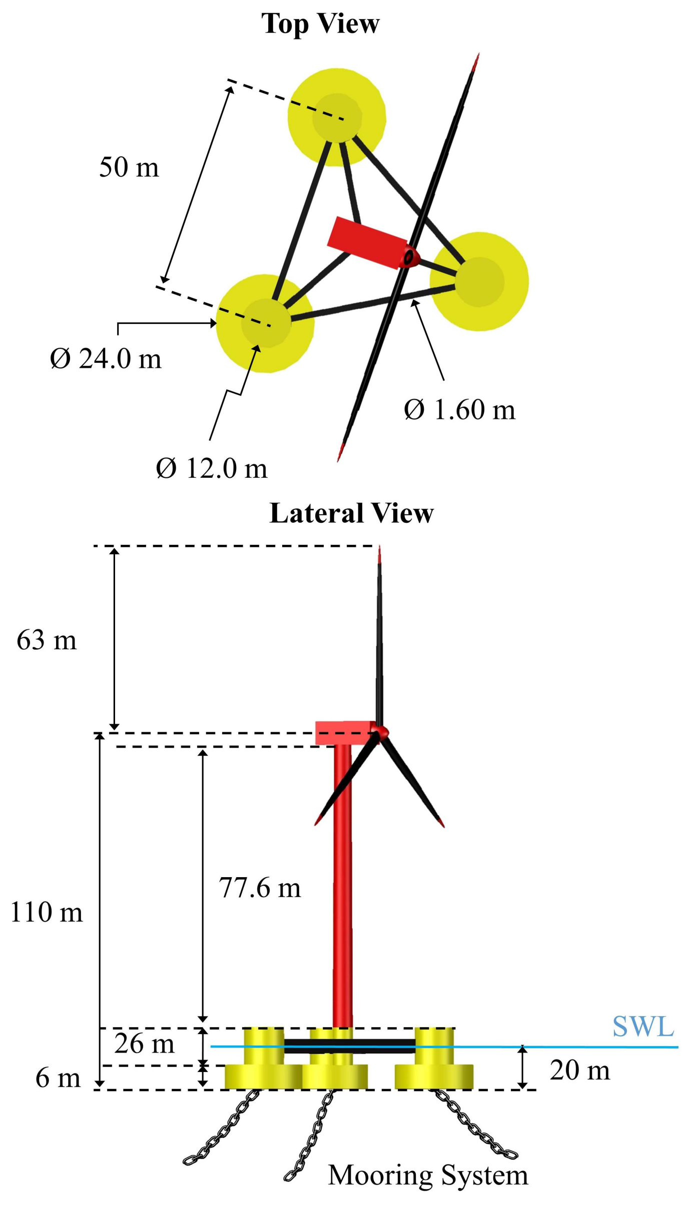

Figure 2.1: NREL's 5 MW baseline offshore WTS with a semi-submersible platform top view and lateral view

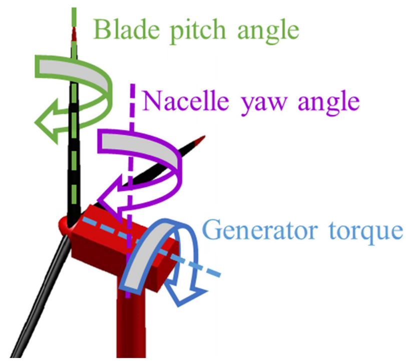

Figure 2.2: Wind turbine control actuators (represented by arrows of different colors) rotating along their degree of freedom (represented by a dashed line)

Table 2.1: Actuator limit values taken from [1]

Control input	Range	Rate limit
Blade pitch angle	-30° to 30°	-8 to 8 deg/s
Generator torque	0 to 47,402 N·m	-15 to 15 kN·m/s
Nacelle yaw angle	-60° to 60°	-0.3 to 0.3 deg/s

speed is 12.1 rpm and is coupled to the generator shaft through a gearbox with a ratio of 97:1. The generator is located upwind with respect to the tower of the system. In order to harvest the energy from the wind, the 5 MW model embodies a variable speed configuration that can operate at a rated torque of 43.1 kN·m applied by the generator. Optimal aerodynamic performance is achieved when applying an active control strategy [39]. The generator torque may vary at a rate of 15 kN·m/s and the generator itself has an electrical efficiency of 94.4%. The control devices are housed in the nacelle, which is located 90 m above the still water level (SWL). The yaw mechanism allows the nacelle to rotate concentrically with the tower such that the system can face the wind direction. This mechanism can rotate at a velocity up to 0.3 deg/s. The wind turbine, including the tower, nacelle, and rotor, weighs approximately 697,460 kg and is attached to a semi-submersible floating platform.

2.1.2 Baseline Offshore Wind Turbine

The specifications of a semi-submersible floating platform were introduced in [40] and are shown in Figure 2.1. The platform is an equilateral triangle of 50 m edge length and it consists of an arrangement of four columns. Outer columns are placed at each vertex of the triangle and are interconnected in a delta configuration by links of 1.6 m diameter. These columns have a height of 26 m and a diameter of 12 m; also, each column is placed on a lower base column with a double sized diameter and a height of 6 m. The three outer lower columns dampen and limit platform motions such as heave, surge, sway, roll and pitch via hydrodynamic drag and inertia. The depth of water needed to float the platform is 20 m. Also, the floating system is ballasted with water located within the outer columns. The main and fourth column is situated at the centerline of the platform and has a diameter of 6.5 m and a height of 30 m. It is linked to the outer structure employing a Y configuration, utilizing the same kind of links. The tower is attached to the main column at a height of 10 m above SWL. The overall calculated mass of the platform is 13.5 kilo-tonnes.

The global reference frame axes are represented by $\hat{x}_g$, $\hat{y}_g$ and $\hat{z}_g$ (the $\hat{z}_g$ axis points in the opposite direction of gravity) and the origin of the global frame is located at the intersection of the wind turbine tower centerline, at its neutral position with no loads, and the SWL. The local reference frame, fixed to the center of gravity of the floating wind turbine, is represented by $\hat{x}_l$, $\hat{y}_l$ and $\hat{z}_l$; the $\hat{z}_l$ axis points toward the tower top. Both the global and the local referee frames are depicted in Figure 2.3. The $\hat{x}_g$ axis faces the wind direction and the $\hat{y}_g$ axis is established according to the right-hand rule. Platform translations in the $\hat{x}_g$, $\hat{y}_g$ and $\hat{z}_g$ directions are referred to as surge, sway, and heave. Platform rotations about these axes are referred to as roll, pitch, and yaw.

The mooring cable system restricts translational and angular motions of the floating platform and consists of three cables. This system is distributed symmetrically around the semi-submersible platform and connects the platform to the seabed. At one end, each cable is connected to the outer cylinders of the semi-submersible platform via a fairlead. At the other end, the cable is attached to an anchor along the seabed at a point located 837.6 m away from the centerline of the

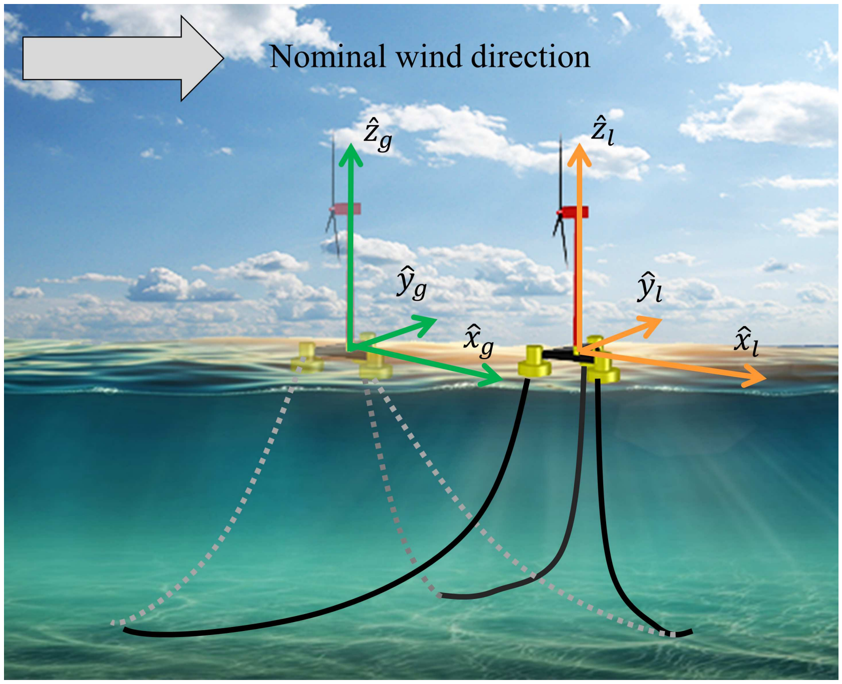

Figure 2.3: The global reference frame (green) located at the neutral position and represented by a transparent wind turbine with dashed mooring lines. The local reference frame (orange) moved along the platform surge due to the effect of the wind direction and represented by a wind turbine with mooring lines of solid colors

platform. Each line is 835.5 m long and has a total mass of 94.7 tonnes. These heavy lines provide restoring forces such that, if the turbine were subject to no loads, would drag the platform back to its neutral position.

2.2 Multi-objective Controller

This section proposes the design of a multi-variable and multi-objective robust controller for controlling the position of an offshore wind turbine. A multi-variable design leads to a tool capable of tackling diverse control goals simultaneously as it enables control of multiple-input multiple-output (MIMO) systems. The controller is designed to manage four different goals; (1) reposition a turbine to a specified location along the $\hat{x}_g$-$\hat{y}_g$ plane, (2) maintain this position under varying wind and wave conditions, (3) maintain a desired rate of electrical energy production while controlling the position of the turbine, (4) minimize angular motions of the platform under varying wind and wave disturbance. These objectives are explained below.

2.2.1 Position Control

This subsection reviews the position control method of an offshore wind turbine developed in [27]. This controller guarantees the relocation and stabilization of a floating platform within a movable area by harnessing the aerodynamic force and the restoring force provided by the mooring line system. Prior to applying this movable control technique, an optimal layout must be derived from the wind farm control level (this task will be addressed in future research at UBC's control engineering lab). This arrangement provides each turbine with a location such that the wake effect is minimized and the power produced from the wind farm is maximal. Then, the offshore WTS makes use of the blade pitch actuator to adjust the backward displacement along the surge direction. This is achieved when modifying the angle of attack of the blade to regulate the thrust force applied by the wind. Similarly, displacement along the sway axis can be accomplished by means of the nacelle yaw mechanism. The selected yaw angle with respect to the nominal wind direction propels the system as if it were a sail. Finally, the restoring force from the mooring lines pulls back the floating platform towards the initial position. As a result, the platform is allowed to be re-positioned anywhere inside a limited region called the movable range. The calculation of this movable range depends on two parameters: the average wind speed velocity and the power generation level. The wind turbine platform may exceed this range temporarily during the transient phase. There is no need for additional actuators besides the collective blade pitch mechanism, generator torque mechanism, and the nacelle yaw mechanism to relocate and maintain the position of an offshore wind turbine within a certain range.

2.2.2 Power Regulation

In addition to calculating the ideal location of each wind turbine, the wind farm controller must also determine the ideal rate at which each turbine extracts energy from the wind. As mentioned in Section 1.3.1, reducing the rate of power extraction of an upstream turbine may increase the wind speed that is incident upon a downstream machine. Therefore, any wind farm control algorithm must consider the rate of power production from each wind turbine in addition to their positions. The third control objective, which is power regulation, ensures that each wind turbine within a wind farm produces the corresponding power set-point established by the wind farm controller.

2.2.3 Angular Velocity Reduction

The slenderness of the massive tower structure of an offshore wind turbine results in a poorly damped system, which induces large pitch and roll motions. It has been found that these platform motions generate significant power fluctuations and tower bending loads [41]. This is corroborated by the International Electrotechnical Commission (IEC), which affirms that angular motions induced in the platform structure as a consequence of hydrodynamic loads indirectly affect the performance of the rotor shaft [42]. Therefore, the reduction of angular motions is a feature cataloged as a “must have” in the employment of wind turbine control systems, since such a controller would improve the safety and structural integrity of the WTS by reducing its risk of failure. The final control objective addresses the reduction of excessive platform angular motions in floating WTS. Specifically, the goal is to minimize platform angular motions while tracking the position and power production set points established by the wind farm controller.

Chapter 3

Mathematical Model and Movable Range

The current chapter is a review of the mathematical models used to design and validate the controller proposed in Section 2.2. For purposes of controller validation, the Fatigue-Aerodynamics-Structures-Turbulence open source code [43], also known as FAST, was used. The theory behind this tool is described in Section 3.1. FAST is an aeroelastic simulator which is able to calculate nominal and fatigue loads of HAWTs of three and two blades. FAST was evaluated by the consulting firm Germanischer Lloyd WindEnergie, which concluded that its accuracy for the evaluation of loads on onshore wind turbines is suitable for design and authentication of structures [44]. For controller design purposes, a control-oriented model described in [45] is introduced in Section 3.2 as a simplified alternative to FAST. Its compromise between simplicity and accuracy compared with the FAST model renders this simplified model a powerful tool for controller design in offshore wind applications. Both models are based on the NREL baseline 5 MW wind turbine defined in Section 2.1. The controller design and validation process is summarized in Figure 3.1. The simplified model is used to design a controller which is then validated using the FAST software. Additionally, the current chapter discusses the movable range of a floating offshore wind turbine in Section 3.2 based on the work by [27]. This movable range indicates to the wind farm controller the limits of the steady position of each wind turbine within a wind farm. The movable range of an offshore WTS is reviewed in Section 3.3.

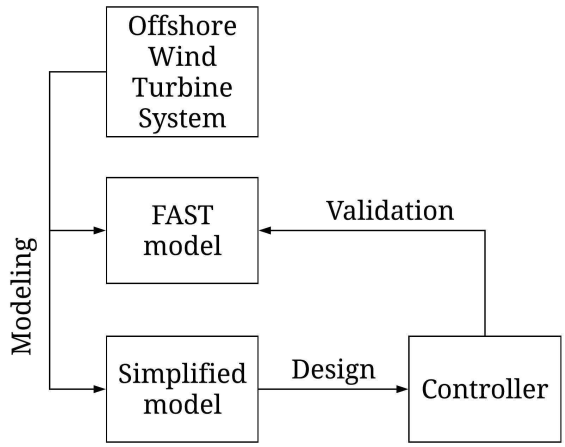

Figure 3.1: Modeling task flowchart of the different wind turbine models employed in this thesis

3.1 FAST Model

FAST solves a system of nonlinear differential equations of motion describing the dynamics of a floating offshore wind turbine. The system of equations is derived using Kane's method. The three-bladed FAST model of a floating offshore wind turbine is characterized by 24 degrees of freedom and includes nine rigid bodies and five flexible bodies. The specific degrees of freedom are listed in Table 3.1, and they result in a total of 44 states. Flexible members are modeled using linear modal dynamic analysis, where the mode shapes of each member are determined offline using a finite element package [46].

A block diagram describing FAST's solver layout is shown in Figure 3.2. The external loads calculated in FAST may be classified under aerodynamic, hydrodynamic, and mooring loads; details and theory are presented in [47]. Aerodynamic loads include the viscous forces acting on the turbine blades and tower. These loads are calculated using FAST's AeroDyn module, which discretizes the blades and tower into smaller segments and uses thin airfoil potential flow theory to calculate the lift and drag forces acting on each segment [48]. Hydrodynamic loads include forces resulting from the interaction of the floating platform with ocean

Table 3.1: List of degrees of freedom of the FAST model

Degree of freedom	Quantity
Translational motion of the platform (surge, sway and heave)	3
Rotational motion of the platform (roll, pitch and yaw)	3
1st and 2nd tower elastic vibration modes (fore-aft and side-side)	4
Nacelle yaw	1
Generator azimuth angle	1
Drivetrain flexibility	1
1st and 2nd blade flapwise vibration modes (first and second mode, three blades)	6
1st blade edgewise vibration mode (three blades)	3
Furling of the rotor and tail	2
Total	24

waves and current. These loads are calculated using FAST's HydroDyn module, which uses a combination of techniques to model waves and their resulting loads caused by fluid-structure interaction [49]. These methods include first and second order potential flow theories to model loads caused by wave diffraction and wave radiation, and strip theory using Morison's equation. HydroDyn also calculates buoyancy forces acting on the floating platform. Finally, the mooring line forces are calculated using FAST's MoorDyn module [50]. MoorDyn models mooring lines as a series of point masses connect via spring and dampers; it is therefore a dynamic mooring line solver. Each point along each mooring line is subject to gravitational, buoyancy, drag, lift, added mass, and ground contact forces. FAST also includes the ServoDyn module, which calculates control signals to the generator, yaw mechanism, and blade pitch actuators. When using FAST via SIMULINK, these control signals may be expressed by the user and serve as inputs into the main FAST module.

FAST offers a linearization feature through which a linearized state-space model may be obtained for controller design purposes. This state-space model includes a linearized wind disturbance matrix, which is a matrix that may be multiplied by

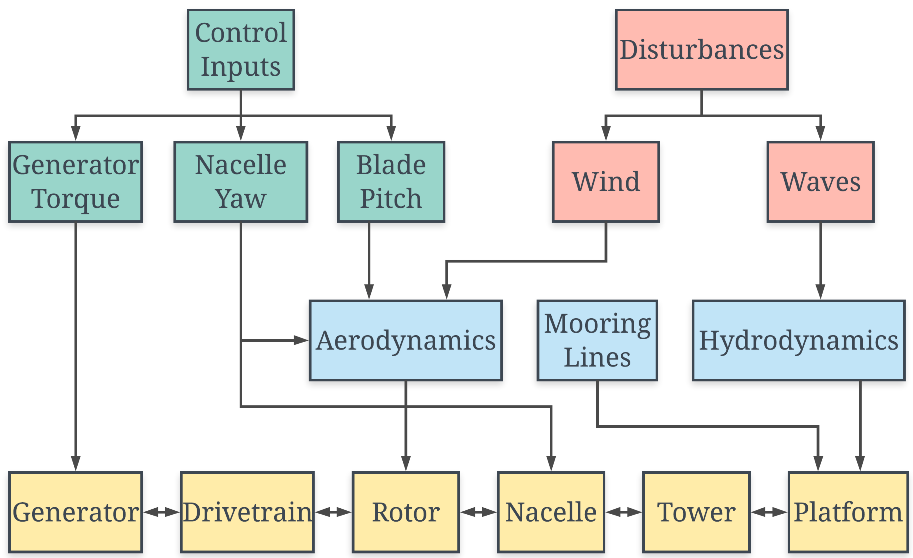

Figure 3.2: Flowchart of the FAST model components and computation

changes in the magnitudes of disturbances relative to an operating point to output the changes in loads acting on the system. FAST does not output a wave disturbance matrix. As a result, the control-oriented floating offshore wind turbine dynamic modeling tool developed by [51], which does output a wave disturbance matrix, is used instead.

3.2 Simplified Model

A simplified non-linear model was developed in our lab as an alternative to the FAST model [45]. This simplified model successfully captures the major dynamic responses of floating offshore wind turbines when compared to FAST; however it requires fewer states and the equations of motion rely on some further simplifying assumptions. The main simplifying assumption is that the entire floating wind turbine is modeled as a single lumped mass, whereas FAST applies Kane's equations to individual bodies (*i.e.* the platform and tower, the nacelle, the main shaft, and the blades). The control-oriented model does not consider flexibility in the turbine

Table 3.2: List of degrees of freedom of the simplified model

Degree of freedom	Quantity
Translational motion of the platform (surge, sway and heave)	3
Rotational motion of the platform (roll, pitch and yaw)	3
Generator azimuth angle	1
Rotor azimuth angle	1
Total	8

tower and blades. An additional simplification is that aerodynamic loads are calculated assuming a collective blade pitch mechanism; that is, all the blade always possess the same pitch angle. Furthermore, the reaction torque generated by yawing the nacelle is ignored; instead, the nacelle yaw angle and yaw rate are directly specified as control inputs. Consequently, the simplified model is characterized by eight degrees of freedom (compared to 24 for FAST), which are listed in Table 3.2.

The equations of motion for the control-oriented dynamic model were derived using a Newtonian approach, where the entire floating wind turbine was treated as a single lumped mass. The equations of motion include three linear momentum conservation equations and three angular momentum conservation equations for the overall mass, and one angular momentum conservation equation for the drivetrain. Similar to FAST, the external loads acting on the system may be classified under aerodynamic, hydrodynamic, and mooring loads; these are shown in Figure 3.3. Rather than using thin airfoil potential flow theory, the control-oriented model utilizes wind turbine rotor performance data to model aerodynamic loads. Parameters include the power, thrust, and torque coefficients of the turbine rotor. This information is calculated offline using FAST's AeroDyn module for a number of different blade pitch angle and tip-speed-ratio settings. Tip-speed-ratio is defined as the ratio of the tip speed of a blade to the wind speed. Once these coefficients are mapped as a function of the collective blade pitch angle (β) and tip-speed-ratio (λ), the overall thrust force acting on the turbine rotor is found using

$$T_{aero} = \frac{1}{2}\rho A v^2 C_T(\lambda, \beta). \tag{3.1}$$

Likewise, the turbine power output is calculated using

$$P_{aero} = \frac{1}{2}\rho A v^3 C_P(\lambda, \beta), \tag{3.2}$$

Finally, the aerodynamic torque driving the turbine rotor is found according to

$$\tau_{aero} = \frac{1}{2}\rho A R v^2 \frac{C_P(\lambda, \beta)}{\lambda}, \tag{3.3}$$

where T_{aero} is the thrust force, P_{aero} is the aerodynamic power, τ_{aero} is the aerodynamic torque, ρ is the air density, A is the swept area of the rotor, and v is the mean wind velocity along the $\hat{x}_g$axis. C_T is the thrust force coefficient, which is the ratio of thrust force to total fluid momentum; similarly, C_P is the power coefficient and denotes the ratio of the power that is harnessed by the wind turbine to the total power in the wind. Based on the simplifying assumptions described earlier, the thrust force is applied at the rotor center. An important property of these equations is that they are steady state. In other words, they neglect transient flow behavior such as boundary layer formation and separation formation. Regardless, these equations are universally used within wind farm control literature.

When calculating hydrodynamic loads, the control-oriented model divides the platform cylinders into three segments and applies Morison's equation to calculate the drag force acting on each segment. Additionally, forces acting on the segment surfaces due to the dynamic wave pressures are calculated. The reason that the cylinders are subdivided into segments is that the wave speed and direction vary along the three dimensional grid. Morison's equation uses drag and added mass coefficients for the cylinder geometries to calculate drag forces and added mass resistance. In addition to these loads, the buoyant forces acting on the cylinders are calculated based on the water pressure normal to the surface of the heave plates. A gravitational force is also applied in the negative $\hat{z}_g$ direction.

Unlike FAST, a static analytical mooring line model is used to calculate mooring line forces. This analytical expression is the solution to the classical mathematical catenary problem under two scenarios; one in which a mooring line partially rests on the seabed, and one in which the entire mooring line is lifted off the seabed. Since these analytical expression, from a nonlinear system of equations, a Newton-Raphson numerical solver is used to calculate the mooring line forces.

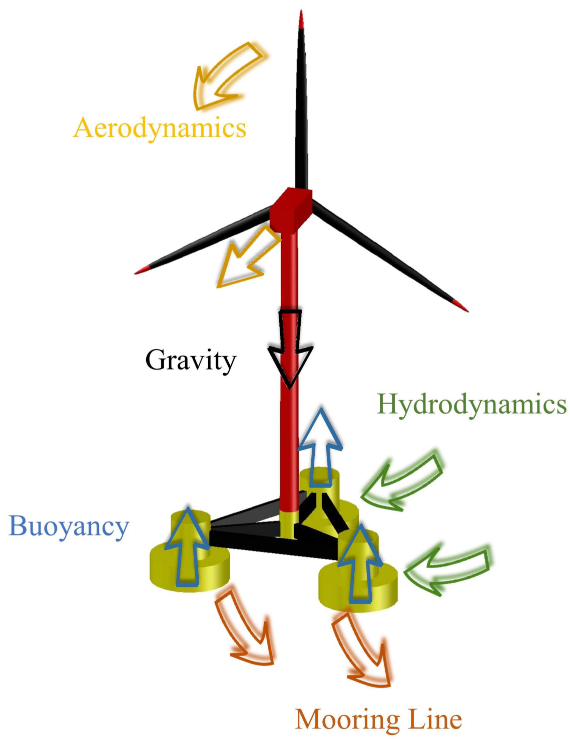

Figure 3.3: Representation of the external loads considered in the derivation of the simplified model

This dynamical nonlinear model can be represented by the state vector $\vec{x}$ as

$$\vec{x} = \begin{bmatrix} \vec{x}_l \\ \vec{\theta}_r \\ \dot{\vec{x}}_l \\ \dot{\vec{\theta}}_r \\ \omega_r \\ \omega_g \\ \Delta\theta \end{bmatrix}, \tag{3.4}$$

where the vector $\vec{x}_l$ is the linear displacement of the floating platform and it consists of the platform surge (x_p), sway (y_p) and heave (z_p). Similarly, the platform rotational displacement vector $\vec{\theta}_r$ contains the platform roll (θ_x), pitch (θ_y) and yaw (θ_z). Furthermore, the linear and rotational velocities $\vec{\dot{x}}_l$ and $\vec{\dot{\theta}}_r$ are described by the derivatives of the previously mentioned states ($\dot{x}_p$, $\dot{y}_p$, $\dot{z}_p$, $\dot{\theta}_x$, $\dot{\theta}_y$ and $\dot{\theta}_z$). For convenience, the rotor and generator azimuth angles are reduced to a single shaft deflection state ($\Delta\theta$). This step is taken because a steady operating point does not exist for the generator and rotor azimuth angles; these angles continue to increase over time. Lastly, the angular velocity of the rotor and generator shafts are represented by ω_r and ω_g, respectively, resulting in a total of 15 states.

The three control inputs of this model are represented by the vector u as

$$\vec{u} = \begin{bmatrix} \beta \\ \tau_g \\ \gamma \end{bmatrix}, \tag{3.5}$$

where β is the collective blade pitch angle, τ_g is the generator torque, and γ is the nacelle yaw angle. Wind disturbances are characterized by the vector v as follows

$$\vec{v} = \begin{bmatrix} v_x \\ v_y \\ v_z \end{bmatrix}, \tag{3.6}$$

where v_x, v_y, and v_z are the wind speeds along the global $\hat{x}_g$, $\hat{y}_g$, and $\hat{z}_g$ axes. The control-oriented model assumes uniform wind speeds; therefore the location of these wind speeds is irrelevant. Wave disturbances are characterized by the vector w as follows

$$\vec{w} = \begin{bmatrix} \vec{w}_1 \\ \vec{w}_2 \\ \vec{w}_3 \\ \vec{w}_4 \end{bmatrix}, \tag{3.7}$$

where $\vec{w}_j$ is the wave disturbance vector for a single platform cylinder. The four wave disturbance vectors correspond to the three outer platform cylinders and the central cylinder. The wave disturbance vector for a single cylinder $\vec{w}_j$ may be further broken down as follows

$$\vec{w}_j = \begin{bmatrix} \vec{w}_{v,j} \\ \vec{w}_{a,j} \\ w_{h,j} \\ \vec{w}_{p,j} \end{bmatrix}, \tag{3.8}$$

where $\vec{w}_{v,j}$ and $\vec{w}_{a,j}$ are the wave velocity and acceleration vectors at cylinder j defined as follows

$$\vec{w}_{v,j} = \begin{bmatrix} v_{wx,j} \\ v_{wy,j} \\ v_{wz,j} \end{bmatrix}, \tag{3.9}$$

$$\vec{w}_{a,j} = \begin{bmatrix} a_{wx,j} \\ a_{wy,j} \\ a_{wz,j} \end{bmatrix}, \tag{3.10}$$

where $v_{wx,j}$, $v_{wy,j}$, and $v_{wz,j}$ are the three-dimensional wave speeds at cylinder j, and $a_{wx,j}$, $a_{wy,j}$, and $a_{wz,j}$ are the three-dimensional wave accelerations at cylinder j. Similar to wind speeds, the control-oriented model assumes uniform wave speeds and accelerations along each cylinder. The scalar term $w_{h,j}$ represents the wave height, defined in the global reference frame, corresponding to the horizontal location of cylinder j. Finally, the vector $\vec{w}_{p,j}$ represents the fluid pressures directly above and below the heave plate of cylinder j as follows

$$\vec{w}_{p,j} = \begin{bmatrix} p_{wt,j} \\ p_{wb,j} \end{bmatrix} \tag{3.11}$$

where $p_{wt,j}$ and $p_{wb,j}$ are the pressures at the top and bottom of the heave plate of cylinder j. Since the heave plates are the only part of the cylinders with faces that are normal to the heave direction, the control-oriented model calculates the dynamic buoyant force on each cylinder as the difference between these top and bottom pressures spread over the heave plate area.

3.3 Movable Range

A final piece of information necessary for designing the controller that has been proposed in this thesis is the movable range of a floating offshore wind turbine. Han [27] utilized the aforementioned control-oriented model to conduct simulations subject to various nacelle yaw angles, blade pitch angles, and wind speeds. Based on the extremes of the turbine's steady settling position, the movable range for a floating offshore wind turbine was defined. Ultimately, the steady settling position is the equilibrium point at which aerodynamic and mooring forces sum to zero. The significance of this movable range is that it informs the wind farm controller of acceptable and feasible turbine position set-points.

Examples of the movable ranges calculated by Han [27] are shown in Figure 3.4; the two plots correspond to different wind speeds. These plots display different movable ranges of a floating offshore wind turbine corresponding to different minimum required power outputs. The first interesting observation is that raising the minimum acceptable power output reduces the movable surge range. This reduction is due to the limited range of thrust forces that will deliver the requisite power output. In other words, in order for the turbine to produce a minimum power of, say 4 MW, a limited range of blade pitch angles is acceptable at each nacelle yaw angle. The second observation is that increasing the wind speed from 15 to 18 m/s increases both the movable surge and sway ranges. This outcome is simply due to the increase in the thrust force caused by higher wind speeds. The movable range may also be expanded by increasing the lengths of the mooring lines. This approach is not considered at this time however.

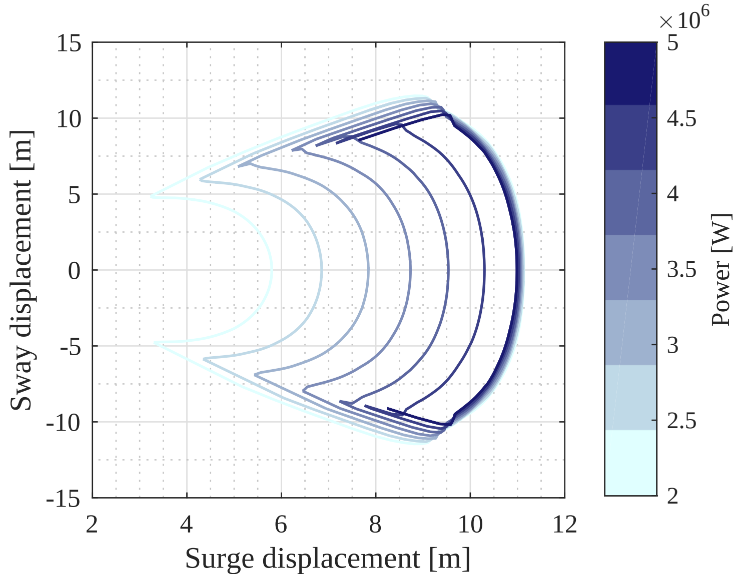

(a) Mean wind velocity of 15 m/s

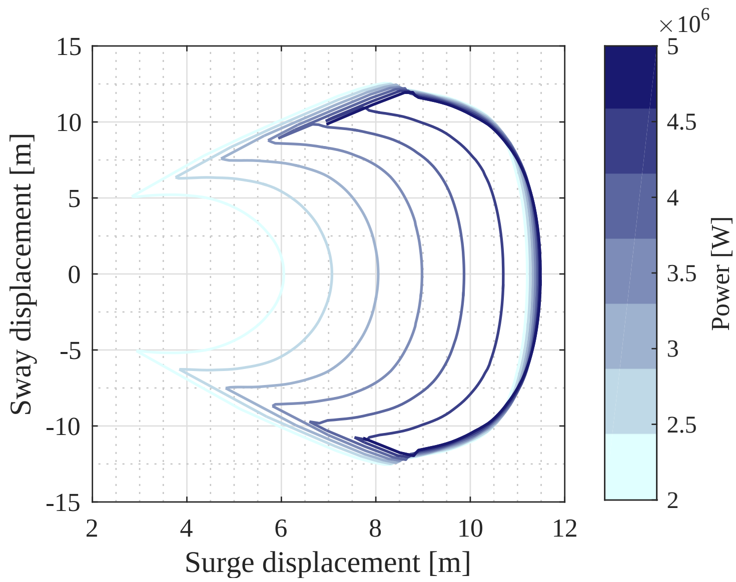

(b) Mean wind velocity of 18 m/s

Figure 3.4: Movable range at diverse power levels assuming a constant mean wind velocity of (a) 15 m/s and (b) 18 m/s

Chapter 4

H_∞ Controller Design

In this chapter, the derivation of the novel multi-objective H_∞ controller is outlined. First, a steady-state equilibrium point is selected and the state, input, and disturbance vectors at this point are computed. The control-oriented dynamic model is then linearized in order to obtain the LTI state, input, and disturbance matrices. Finally, an H_∞ controller is designed utilizing the linear matrix inequality (LMI) technique.

4.1 System Analysis

4.1.1 Equilibrium Point Selection and Computation

In Section 3.2, a non-linear control-oriented model of the following form was described

$$\dot{\vec{x}} = f(\vec{x}, \vec{u}, \vec{v}, \vec{w}). \tag{4.1}$$

The following step involves establishing a steady-state operating point vector $\vec{p}$. This vector consists of the equilibrium state ($\vec{x}^*$), input ($\vec{u}^*$), and disturbance ($\vec{v}^*$ and $\vec{w}^*$) vectors computed at the selected operating point as follows

$$\vec{p} = \begin{bmatrix} \vec{x}^* \\ \vec{u}^* \\ \vec{v}^* \\ \vec{w}^* \end{bmatrix}. \tag{4.2}$$

Since these states are computed at a steady operating point, the derivatives of the states are zero as follows

$$f(\vec{x}^*, \vec{u}^*, \vec{v}^*, \vec{w}^*) = \vec{\dot{x}}^* = \vec{0}. \tag{4.3}$$

The operating point is calculated based on the target positions $x_{p,tar}$ and $y_{p,tar}$ and the target power production P_{tar} that would hypothetically be determined by a wind farm controller. With these targets established, the remaining states and inputs were found using the Newton-Raphson method. As for the disturbance vectors, a wind speed of 18 m/s in the global $\hat{x}_g$ direction and wave speeds, accelerations, dynamic pressures, and heights of zero (*i.e.* still water with no turbine heave) were specified to obtain the operating point. The wind speed of 18 m/s was selected because it ensured a maximum power production of 5 MW and because movable range data for this wind speed was available from previous work. Additionally, previous controllers have been designed for this wind turbine system at a wind speed of 18 m/s; the performance of the H_∞ controller designed in this thesis could therefore be compared to the performance of these existing controllers. Setting the wave disturbances to zero was deemed appropriate since wave velocities are oscillatory and their directions therefore fluctuate around zero.

The generator torque at the operating point τ_g^* was related to the target power production using the following equilibrium equation

$$\tau_g^* = \frac{P_{tar}}{\eta_g \omega_g}, \tag{4.4}$$

where η_g is the efficiency of the generator. The total number of unknowns to be solved using the Newton-Raphson method therefore amounted to 16. These include 13 states (*i.e.* 15 initial states minus the turbine surge and sway that have been specified beforehand) and three inputs (*i.e.* the collective blade pitch angle, the generator torque and the nacelle yaw angle,). The vector ψ is defined to contain these unknowns as follows

$$\vec{\psi} = [z_p^*, \theta_x^*, \theta_y^*, \theta_z^*, \dot{x}_p^*, \dot{y}_p^*, \dot{z}_p^*, \dot{\theta}_x^*, \dot{\theta}_y^*, \dot{\theta}_z^*, \omega_r^*, \omega_g^*, \Delta\theta^*, \beta^*, \tau_g^*, \gamma^*]^T. \tag{4.5}$$

The 16 equations necessary to solve for these unknowns consist of 15 state equations from Eq. (4.1) and the generator torque equation from Eq. (4.4).

4.1.2 Linearization Calculation

With the operating point established and the states and inputs at this point, deviations in the states, inputs, and disturbances from the operating point values were defined using the symbol δ as follows

$$\delta\vec{x} = \vec{x} - \vec{x}^* \tag{4.6}$$

$$\delta\vec{u} = \vec{u} - \vec{u}^* \tag{4.7}$$

$$\delta\vec{v} = \vec{v} - \vec{v}^* \tag{4.8}$$

$$\delta\vec{w} = \vec{w} - \vec{w}^*. \tag{4.9}$$

The linearized model was then found by implementing a first-order Taylor series approximation of the nonlinear system of equations about the operating point p as follows

$$\delta\dot{\vec{x}} = \left.\frac{\partial f}{\partial \vec{x}}\right|_{\vec{p}} \delta\vec{x} + \left.\frac{\partial f}{\partial \vec{u}}\right|_{\vec{p}} \delta\vec{u} + \left.\frac{\partial f}{\partial \vec{v}}\right|_{\vec{p}} \delta\vec{v} + \left.\frac{\partial f}{\partial \vec{w}}\right|_{\vec{p}} \delta\vec{w}, \tag{4.10}$$

which represents a linear and time-invariant differential equation. Also, the linearized system matrices were defined from this solution as follows

$$\begin{aligned} \mathbf{A} &= \left.\tfrac{\partial f}{\partial \vec{x}}\right|_{\vec{p}}, \quad & \mathbf{B} &= \left.\tfrac{\partial f}{\partial \vec{u}}\right|_{\vec{p}} \\ \mathbf{B}_v &= \left.\tfrac{\partial f}{\partial \vec{v}}\right|_{\vec{p}}, \quad & \mathbf{B}_w &= \left.\tfrac{\partial f}{\partial \vec{w}}\right|_{\vec{p}}, \end{aligned} \tag{4.11}$$

where $\mathbf{A}$ is the state matrix, $\mathbf{B}$ is the input matrix, $\mathbf{B}_v$ is the wind disturbance matrix, and $\mathbf{B}_w$ is the wave disturbance matrix. Since the proposed H_∞ controller uses state-feedback, the output is simply defined as

$$\vec{y} = \vec{x}.$$

In summary, the linearized system of dynamic state-space equations is represented as a block diagram in Figure 4.1 and takes the following form

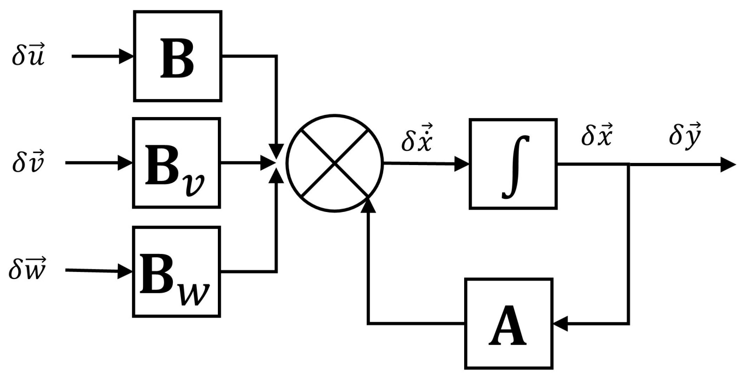

Figure 4.1: Block diagram resultant from the linearization of the control-oriented model

$$\delta\dot{\vec{x}} = \mathbf{A}\delta\vec{x} + \mathbf{B}\delta\vec{u} + \mathbf{B}_v\delta\vec{v} + \mathbf{B}_w\delta\vec{w} \tag{4.12}$$

$$\delta\vec{y} = \delta\vec{x}. \tag{4.13}$$

where only the system coefficient matrices $\mathbf{A}$, $\mathbf{B}$, $\mathbf{B}_v$, and $\mathbf{B}_w$ are of importance for designing the proposed H_∞ controller.

4.2 Control Design

In this section, the structure of the proposed controller is presented. Two controllers are employed to achieve the desired performance of a WTS in accordance with the objectives defined in Section 2.2. A state-feedback controller is first designed based on the H_∞ method. The objective of this controller is to regulate the position and power of the WTS and to minimize its angular motion, all by only actuating the nacelle yaw angle γ and the collective blade pitch angle β. The generator torque τ_g is regulated using a constant power strategy defined as follows

$$\tau_g = \frac{P_{tar}}{\eta_g \omega_g}. \tag{4.14}$$

A block diagram for the overall control system is shown in Figure 4.2. The block designated as K_τ implements the constant power strategy from Eq. (4.14). The matrix $\mathbf{L}$ extracts the generator angular speed ω_g from the state vector. This

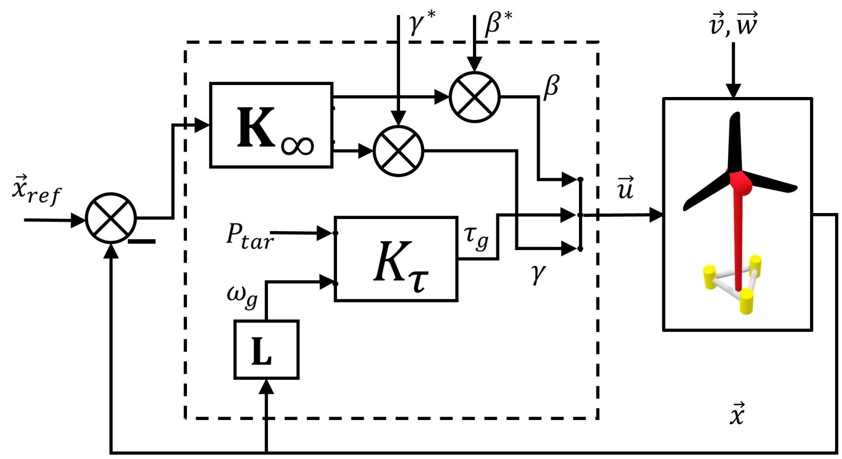

Figure 4.2: Proposed control block diagram

controller operates in parallel with the H_∞ controller whose gain value is denoted by the $\mathbf{K}_\infty$ block. This gain is multiplied by the error signal that is calculated as the measured state vector $\vec{x}$ subtracted from the reference signal $\vec{x}_{ref}$, which contains the target commands for the wind turbine.

4.2.1 H_∞ Control Description

The benefit of implementing a robust control system is that it guarantees desired performance specifications in the presence of noise, model uncertainty and disturbances. This characteristic is particularly useful for floating offshore wind turbine applications since the primary causes of platform angular motion are fluctuations in wind and wave disturbance. As a result, the robust controller designed in this thesis is an H_∞ controller, which is powerful for rejecting disturbances to meet performance specifications.

A brief overview of the H_∞ controller design methodology is now given. The H_∞ norm is the maximum singular value of a transfer function over an infinite frequency range. For single-input single-output systems, the H_∞ norm is simply the maximum value of a scalar transfer function over an infinite frequency range. For multiple-input multiple-output systems, the H_∞ norm is the maximum matrix norm of a matrix transfer function over an infinite frequency range. The objective of H_∞ controller design is to minimize this H_∞ norm for a closed-loop system. In this thesis, the transfer functions that are used to compute the H_∞ norm are referred to as sensitivity functions S, which are the transfer functions from disturbances to outputs. As a result, the ultimate goal of an H_∞ controller is to minimize the gain in the outputs of a closed-loop systems in response to fluctuations in disturbances.

Reduction of disturbance influence between different performance channels is achieved by multiplying them by weighting functions $\mathbf{W}_f$. These weighting functions may be used as a trade-off to emphasize desired performance channels. For the H_∞ controller designed in this thesis, constant weighting functions were implemented. These weighting functions therefore established an upper limit on the H_∞ norm at all frequencies.

4.2.2 H_∞ Controller Design

The first step in designing the H_∞ controller involved defining the vector ϕ, which contains the states whose perturbations in response to disturbance must be minimized. The vector $\vec{\phi}$ is defined as follows

$$\delta\vec{\phi} = \begin{bmatrix} \delta x_p \\ \delta y_p \\ \delta\omega_g \\ \delta\dot{\theta}_x \\ \delta\dot{\theta}_y \end{bmatrix}, \tag{4.15}$$

where δx_p and δy_p denote fluctuations in the turbine position from the target position, $\delta\omega_g$ denotes fluctuations in the generator speed from the designated operating point, and $\delta\dot{\theta}_x$ and $\delta\dot{\theta}_y$ denote fluctuations in the roll and pitch angular velocities of the turbine platform from an operating point value of zero. The goal is to design an H_∞ controller to minimize the vector $\vec{\phi}$ while guaranteeing stability of the closed-loop system.

Since the generator torque τ_g was calculated using the constant power strategy from Eq. (4.14), the input vector for H_∞ controller design was altered to

$$\delta\vec{u}' = \begin{bmatrix} \delta\beta \\ \delta\gamma \end{bmatrix}, \tag{4.16}$$

and the linearized input matrix was altered accordingly. This new input matrix is denoted by $\mathbf{B}'$. After this, the system may be described in the following linearized state-space form

$$\delta\dot{\vec{x}} = \mathbf{A}\delta\vec{x} + \mathbf{B}_v\delta\vec{v} + \mathbf{B}_w\delta\vec{w} + \mathbf{B}'\delta\vec{u}'. \tag{4.17}$$

The next step involves weighting the vectors $\delta\vec{\phi}$ and $\delta\vec{u}'$ in order to establish their effect on the optimization output. This weighting is implemented using the matrices $\mathbf{W}_\phi$ and $\mathbf{W}_{u'}$ as follows

$$\delta\vec{\phi}_w = \mathbf{W}_\phi\mathbf{C}_0\delta\vec{x}, \tag{4.18}$$

$$\delta\vec{u}'_w = \mathbf{W}_{u'}\delta\vec{u}'. \tag{4.19}$$

$\mathbf{W}_\phi$ and $\mathbf{W}_{u'}$are the tuning parameters for the controller. The $\mathbf{C}_0$ matrix has dimensions of 5×15 and extracts only the states from the vector $\delta\vec{x}$ that are part of the vector $\delta\vec{\phi}$ shown in Eq. (4.15).

Defining an augmented plant as

$$\begin{bmatrix} \delta\dot{\vec{x}} \\ \delta\vec{\phi}_w \\ \delta\vec{u}'_w \end{bmatrix} = \begin{bmatrix} \mathbf{A} & \mathbf{B}_v & \mathbf{B}_w & \mathbf{B}' \\ \mathbf{W}_\phi\mathbf{C}_0 & \mathbf{0} & \mathbf{0} & \mathbf{0} \\ \mathbf{0} & \mathbf{0} & \mathbf{0} & \mathbf{W}_{u'} \end{bmatrix} \begin{bmatrix} \delta\vec{x} \\ \delta\vec{v} \\ \delta\vec{w} \\ \delta\vec{u}' \end{bmatrix} \tag{4.20}$$

where the augmented plant matrix may be defined as follows

$$\mathbf{M}_{aug} = \begin{bmatrix} \mathbf{A} & \mathbf{B}_v & \mathbf{B}_w & \mathbf{B}' \\ \mathbf{W}_\phi\mathbf{C}_0 & \mathbf{0} & \mathbf{0} & \mathbf{0} \\ \mathbf{0} & \mathbf{0} & \mathbf{0} & \mathbf{W}_{u'} \end{bmatrix}, \tag{4.21}$$

such that the augmented plant yields the system of equations consisting of Eq. (4.17) to Eq. (4.19). These equations relate the fluctuations in the weighted states and in-

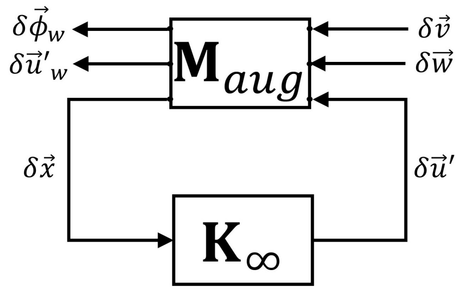

Figure 4.3: Block diagram of the H_∞ controller closed-loop system employing the augmented plant $\mathbf{M}_{aug}$. The aim of the H_∞ controller is to reduce the effect of wind ($\delta\vec{v}$) and wave ($\delta\vec{w}$) disturbances on the performance of the weighted channels $\delta\vec{\phi}_w$ and $\delta\vec{u}_w$

puts (*i.e.* $\delta\vec{\phi}_w$ and $\delta\vec{u}_w$) to changes in disturbances (*i.e.* $\delta\vec{v}$ and $\delta\vec{w}$) as shown in Figure 4.3.

The final step involves using the LMI technique to determine the optimal H_∞ controller gain. LMI is a convex optimization technique that is commonly used for H_∞ controller design due to its efficiency and numerical reliability [52]. First, the following matrices are defined in accordance with the LMI technique requirements

$$\mathbf{B}_1 = \begin{bmatrix} \mathbf{B}_v & \mathbf{B}_w \end{bmatrix} \tag{4.22}$$

$$\mathbf{B}_2 = \mathbf{B}' \tag{4.23}$$

$$\mathbf{C} = \begin{bmatrix} \mathbf{W}_\phi \mathbf{C}_0 \\ \mathbf{0} \end{bmatrix} \tag{4.24}$$

$$\mathbf{D}_1 = \mathbf{0} \tag{4.25}$$

$$\mathbf{D}_2 = \begin{bmatrix} \mathbf{0} \\ \mathbf{W}_{u'} \end{bmatrix} \tag{4.26}$$

As stated in [52], the LMI technique attempts to minimize the scalar ζ by calculating optimal values for a matrix $\mathbf{W}$ and a symmetric positive definite matrix $\mathbf{X}$. The scalar ζ is therefore the H_∞ norm, the inverse of $\mathbf{X}$ is the Lyapunov stability matrix, and $\mathbf{W}$ is an intermediary matrix necessary for obtaining a linear matrix inequality.

The LMI technique then involves solving the following optimization problem

$$\begin{cases} \min & \zeta \\ \text{so that} & \mathbf{X} > \mathbf{0} \\ & \begin{bmatrix} (\mathbf{AX}+\mathbf{B}_2\mathbf{W})^T + \mathbf{AX}+\mathbf{B}_2\mathbf{W} & \mathbf{B}_1 & (\mathbf{CX}+\mathbf{D}_2\mathbf{W})^T \\ \mathbf{B}_1^T & -\zeta\mathbf{I} & \mathbf{D}_1^T \\ \mathbf{CX}+\mathbf{D}_2\mathbf{W} & \mathbf{D}_1 & -\zeta\mathbf{I} \end{bmatrix} < \mathbf{0}. \end{cases} \tag{4.27}$$

to determine optimal $\mathbf{W}$ ($\mathbf{W}_{opt}$) and $\mathbf{X}$ ($\mathbf{X}_{opt}$) matrices. The H_∞ controller gain is the defined as

$$\mathbf{K}_\infty = \mathbf{W}_{opt}\mathbf{X}_{opt}^{-1}. \tag{4.28}$$

The optimization problem was solved using MATLAB's LMI tool, which is part of its robust control toolbox [53].

The control scheme including both the H_∞ and constant power torque controllers is depicted in Figure 4.4. The value set for the scalar weighting functions as well as the gains K_τ and $\mathbf{K}_\infty$ are listed in Appendix A.

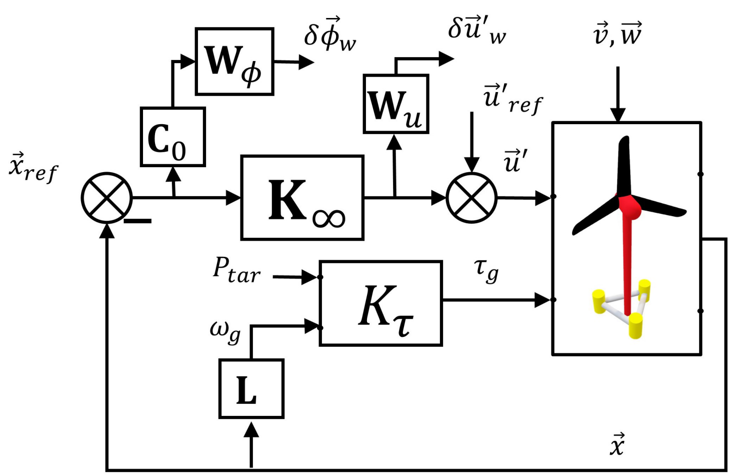

Figure 4.4: Control block diagram utilizing the the proposed H_∞ controller along with the constant power strategy

Chapter 5

Simulation Results

5.1 Simulation Framework

The H_∞ controller described in Chapter 4 is validated in the time-domain using NREL's FAST software. Realistic unsteady wind and wave profiles are implemented within the simulation, and control input limits such as saturation and rate limits are employed as previously mentioned in Table 2.1. Three different simulations were carried out to assess different characteristics of the H_∞ controller. In Section 5.2, the H_∞ controller is compared to an LQI controller while relocating a floating wind turbine between two points at constant power production. In Section 5.3, the effectiveness of the H_∞ controller in sequentially relocating a floating turbine to multiple points while being subject to varying power production targets is assess. In Section 5.4, the robustness of the H_∞ controller is assessed against increased wind speed and wave height, again in comparison with an LQI controller.

5.1.1 Wind Profile

Turbulent wind speed profiles were generated using FAST's TurbSim module [54]. TurbSim is a numerical simulator of turbulent and stochastic wind. It generates three dimensional turbulent wind velocity profiles (v_x, v_y, v_z) that serve as inputs to FAST's AeroDyn module (a brief description of AeroDyn is provided in Section 3.1). The data generated by TurbSim consists of a mean wind speed in the positive global $\hat{x}_g$ direction with velocity fluctuations in all three dimensions. As shown in Figure 5.1, the average wind speed value around the turbine hub height is 18 m/s along the $\hat{x}_g$ direction with turbulent velocity fluctuations based on a normal turbulence model (NTM) of intensity C.

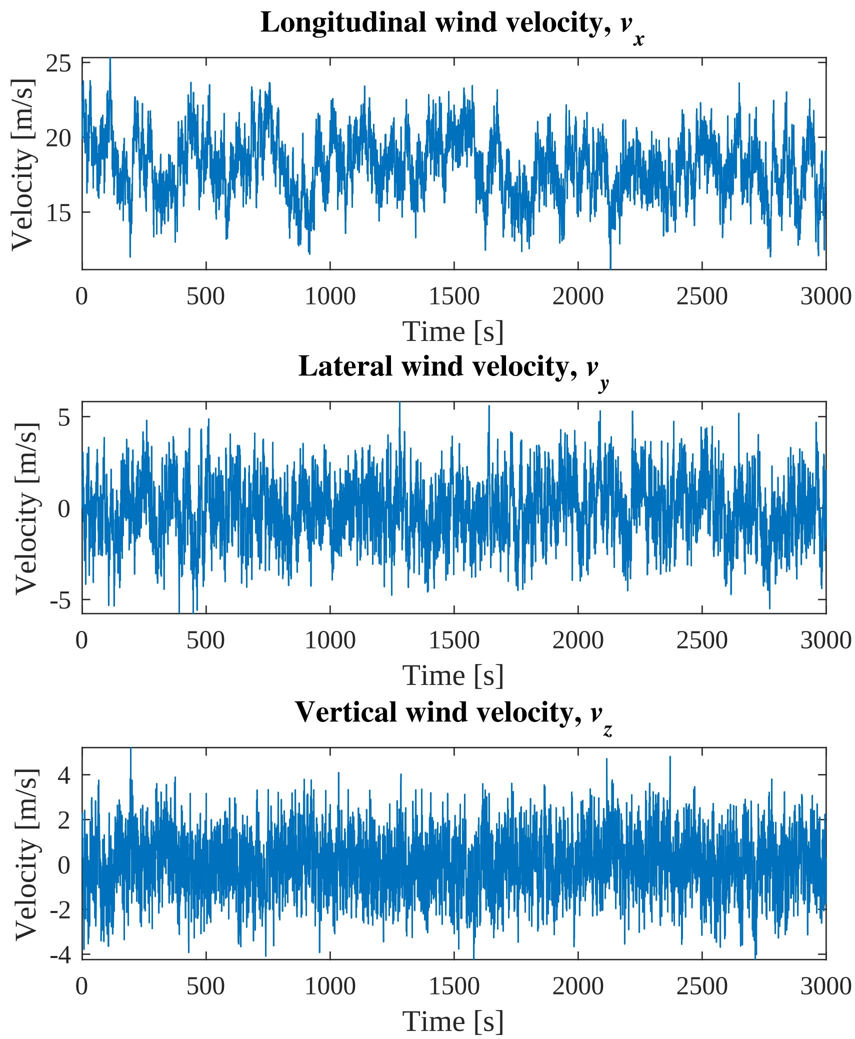

Figure 5.1: Turbulent realistic wind profile generated by TurbSim

5.1.2 Wave Profile

FAST's HydroDyn module generates irregular wave velocity and elevation profiles based on the JONSWAP/Pierson-Moskowitz wave spectrum. The generated wave data for simulations are shown in Figure 5.2; these graphs show the wave elevation and velocity at a single cylinder of the floating turbine. The maximum elevation of the incident waves was 5 m, with a peak spectral period of 12.4 s. The predominant direction of wave propagation matches the predominant wind direction; thus, w_y is relatively small compared to w_x.

5.2 Regulation Comparison H_∞ vs LQI

The proposed H_∞ controller was first compared to an LQI controller in order to assess the benefits of utilizing robust control in systems with significant disturbance. Similar to the H_∞ approach, LQI control is a multi-objective and multi-variable control technique. However, the difference is that H_∞ control considers disturbance information during controller design process. For the comparison, the controllers were tasked with repositioning the floating wind turbine from an initial position $(x_{p,i}, y_{p,i})$ to a target position $(x_{p,tar}, y_{p,tar})$, and then maintaining the turbine at this location. During these two processes, the regulation of the target power (P_{tar}) and the reduction of the angular motion of the platform served as additional control objectives.

The initial point was located at $(x_{p,i} = 11$ m, $y_{p,i} = 0$ m), which corresponds to the turbine being initially located 11 m downstream from its neutral position. The target position was set to $(x_{p,tar} = 8$ m, $y_{p,tar} = 8$ m) and the power production target was set to $P_{tar} = 3$ MW. These targets and initial points are similar to those implemented in a previous study by [28]. Time-domain simulations were conducted for 3000 s (50 min) using the wind and wave profiles in Figures 5.1 and 5.2.

In order to focus the comparison between the two controllers on the angular motion, the H_∞ controller parameters were tuned such that the root-mean-square error (RMSe) corresponding to its power output matched the power output RMSe of the LQI controller. The RMSe is a singular value measure of the error between a noisy signal and its mean value. For a discrete signal $\vec{a}$ of k elements that deviate

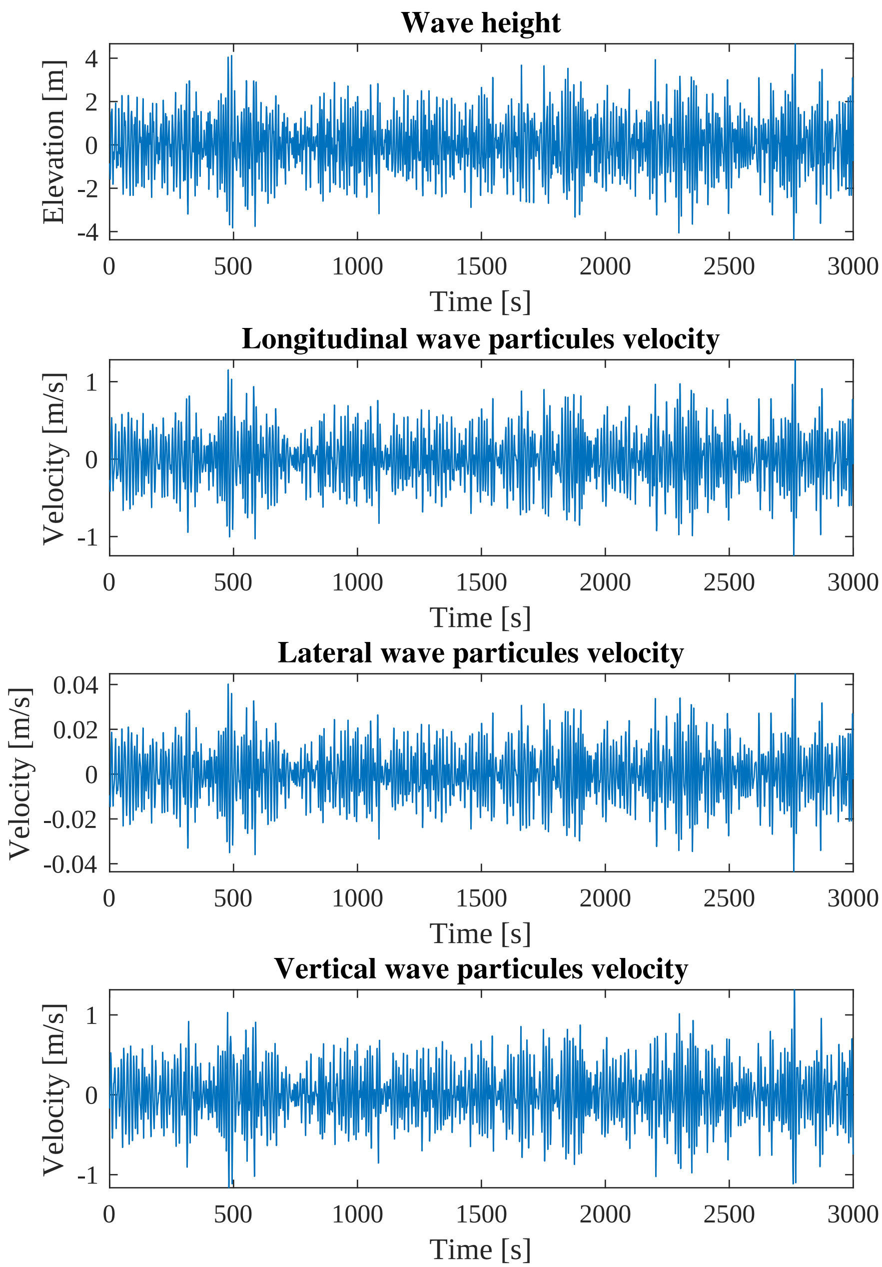

Figure 5.2: Stochastic wave profile generated by HydroDyn

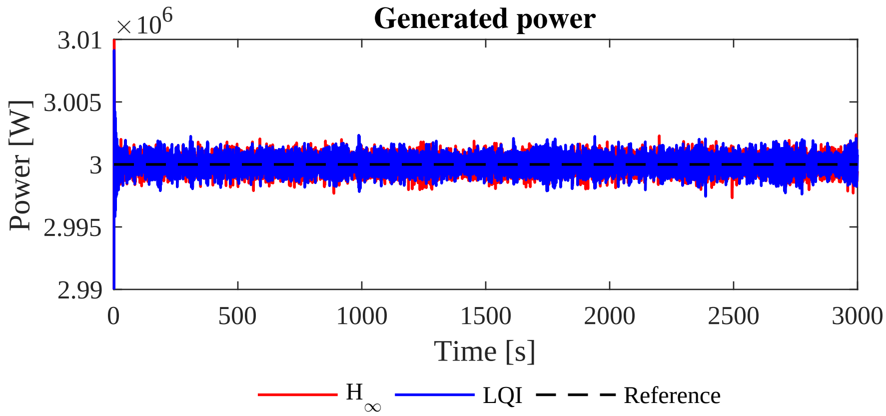

Figure 5.3: Comparison of wind turbine power output obtained using the H_∞ and LQI controllers. Tuned parameters for the H_∞ and LQI controllers are listed in Appendix A.1

from the mean value $\vec{a}_{ref}$, the RMSe is calculated as follows

$$RMSe = \sqrt{\frac{\sum_{n=1}^{k}(\vec{a}_n - \vec{a}_{ref})^2}{k}}$$

In this case, $\vec{a}_{ref}$ was set equal to P_{tar} = 3 MW.

The time-domain power output responses for both controllers are displayed in Figure 5.3. Both controllers successfully tracked the target value of 3 MW. The RMSe values obtained from the H_∞ and LQI controllers after tuning the H_∞ controller were 586 W and 594 W, respectively. The turned parameters for the LQI controller were obtained from [27].

The surge (x_p) and sway (y_p) time-domain responses are plotted in Figure 5.4. Focusing on platform surge, the maximum overshoot for the H_∞ and LQI controllers as a percentage of mean values were 56.20 and 63.48 %, respectively; the maximum overshoot for the H_∞ controller was therefore 7.28 % smaller than that of the LQI controller. The time necessary for surge fluctuations about mean values to stabilize was approximately 165 s for both controllers. Beyond this point, the largest peak-to-peak fluctuation as a percentage of mean value for the H_∞ controller was 52.60 %; this value was 57.16 % for the LQI controller. The maximum peak-to-peak fluctuation as a percentage of mean value for the H_∞ controller was therefore 4.56 % smaller than that of the LQI controller. The mean surge value maintained by the H_∞ controller was 4.68 % greater than the target surge position of 8 m; the LQI controller offered better surge tracking performance with a mean surge value that was 0.1 % smaller than the target surge position of 8 m. Although the H_∞ controller was inferior in terms of tracking the target surge position, it offer improved performance in terms of angular velocity reduction.

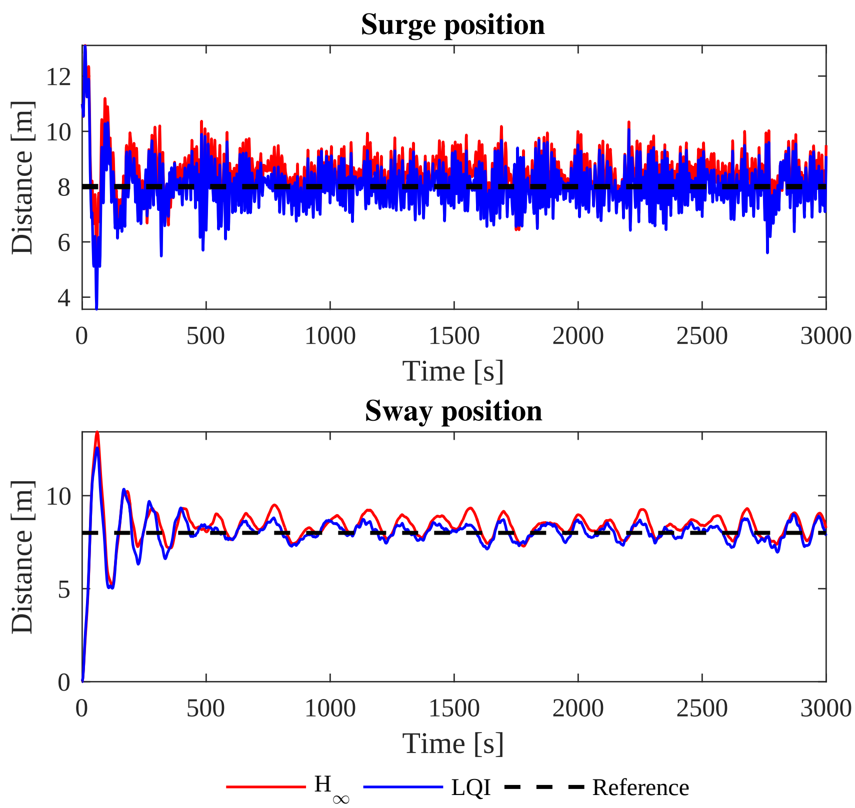

Figure 5.4: Comparison of wind turbine surge and sway motions obtained using the H_∞ and LQI controllers. Tuned parameters for the H_∞ and LQI controllers are listed in Appendix A.1

The roll and pitch angular velocity time-domain responses are plotted in Figure 5.5. The RMSe values for roll angular velocities corresponding to the H_∞ and LQI controllers were 0.066 and 0.110 deg/s, respectively; the H_∞ controller therefore reduced mean roll angular velocity values by 40 %. Pitch angular velocity RMSe values were approximately the same at 0.245 deg/s for the for the H_∞ controller and 0.241 deg/s for the LQI controller, and this pattern persisted regardless of the weighting coefficients used. This behavior is due to the fact that it is primarily the collective blade pitch angle that may be used to alter the platform pitching moment, however doing so conflicts with the objectives of surge position control and power tracking. In comparison, altering the nacelle yaw angle primarily influences the platform sway position and the rolling moment, it has little effect on power production and surge motion; hence the reason that the H_∞ controller is capable of altering the yaw angle to minimize roll angular velocity without conflicting with other control objectives. On the other hand, altering the collective blade pitch angle has a significant impact on both the surge motion and power production; therefore the H_∞ controller's capacity to vary the collective blade pitch angle in order to minimize the platform's pitching motion is limited.

Referring back to Figure 5.4 to examine the platform's sway motion, the maximum sway overshoot for the H_∞ and LQI controllers as a percentage of mean values were 60.43 and 56.21 %, respectively; the maximum overshoot for the H_∞ controller was therefore 4.22 % greater than that of the LQI controller. The H_∞ controller's inferior performance when concerned with maximum sway overshoot is due to the conflicting objective of minimizing roll motion. Minimizing the roll motion requires that sudden and significant changes in the rolling moment be limited; therefore the controller's ability to counter sway overshoot is also limited. The time necessary for sway fluctuations about mean values to stabilize was approximately 415 s for both controllers. Beyond this point, peak-to-peak fluctuations as a percentage of mean values were approximately the same at 26 % for both controllers. As with surge control, the H_∞ controller was inferior when concerned with tracking the sway set-point. The mean sway value maintained by the H_∞ controller was 4.68 % greater than the target sway position of 8 m; this value was 0.68 %. The inferior position tracking of the H_∞ controller, concerning both surge and sway, is due to its additional objectives of minimizing angular motion.

The generator angular speed time-domain responses for both controllers are plotted in Figure 5.6. Since the H_∞ controller was designed to minimize fluctuations in the generator angular speed from the operating speed of 105.153 deg/s, it

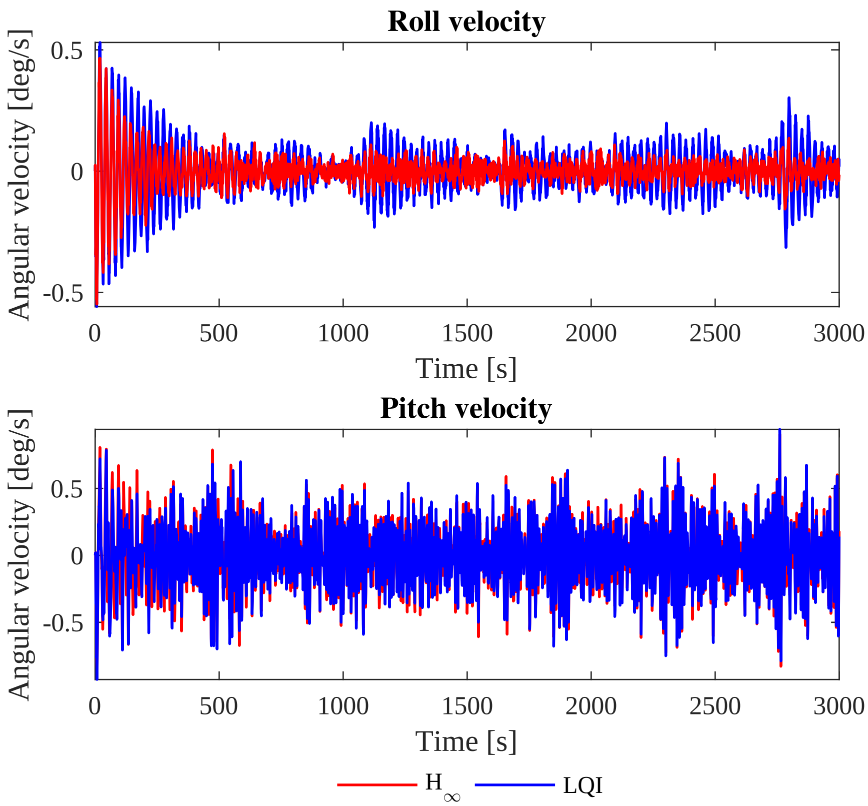

Figure 5.5: Comparison of wind turbine roll and pitch velocities obtained using the H_∞ and LQI controllers. Tuned parameters for the H_∞ and LQI controllers are listed in Appendix A.1

did so more effectively than the LQI controller with a mean value of 104.409 deg/s; the mean generator speed for the LQI controller was 101.382 deg/s. The RMSe value of the generator speeds were 1.670 deg/s for the H_∞ controller and 1.694 deg/s for the LQI controller. These values correspond to a 1.41 % reduction in RMSe when using the H_∞ controller. Additionally, the H_∞ controller prevented some the larger spikes in the LQI controller's generator angular speed that are visible at simulation times of $t = 33$ s and $t = 2776$ s.

Time-domain control signals from the H_∞ and LQI controllers are plotted in Figure 5.7. Since the H_∞ controller yielded a greater generator speed than that of the LQI controller, its generator torque was decreased in order to maintain power

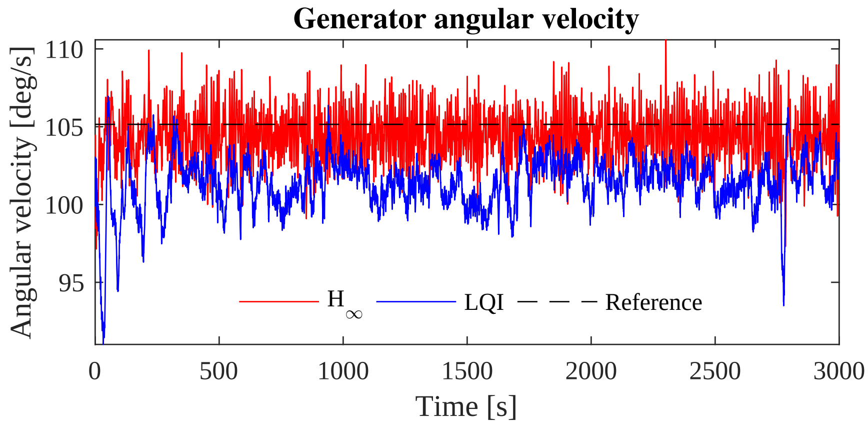

Figure 5.6: Comparison of generator shaft angular speed obtained using the H_∞ and LQI controllers. Tuned parameters for the H_∞ and LQI controllers are listed in Appendix A.1

output. The resulting mean generator torques for the H_∞ and LQI controllers were 30.45 and 31.35 kN·m. The mean collective blade pitch angle for the H_∞ controller was also greater in the stall (*i.e.* negative) direction as a result of this generator torque difference. An increase in the blade pitch angle, in either the stall or feather directions, reduces the aerodynamic torque acting on the wind turbine rotor. Since the generator torque must match the aerodynamic torque under steady operating conditions, and the generator torque for the H_∞ controller was 2.87 % lower than that of the LQI controller, the mean collective blade pitch angle for the H_∞ controller was 5.51 % greater than that of the LQI controller. The mean collective blade pitch angles were -7.731 and -7.327 deg for the H_∞ and LQI controllers, respectively. Higher blade pitch angles in the stall direction also serve to increase the overall thrust force acting on the turbine rotor. Since the turbine rotor under H_∞ control operation possessed a larger blade pitch angle in the stall direction, a smaller mean nacelle yaw angle was necessary to reach the target sway position. This is why the mean nacelle yaw angles for the H_∞ and LQI controllers were 35.721 and 36.427 deg.

Overall, the H_∞ controller offered improved performance in terms of reducing platform roll angular velocity relative to an LQI controller; specifically, a 40 % reduction was achieved. This outcome must be accompanied by greater fluctuations

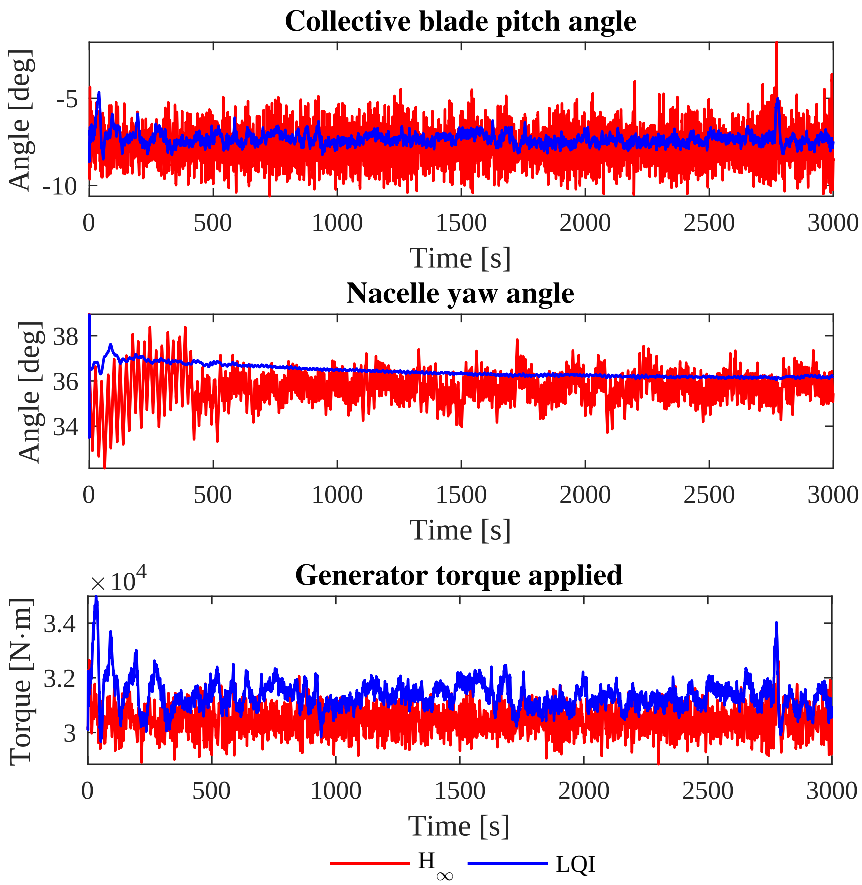

Figure 5.7: Comparison of wind turbine control inputs obtained using the H_∞ and LQI controllers. Tuned parameters for the H_∞ and LQI controllers are listed in Appendix A.1

in the control signals however, since more variation in blade pitch and nacelle yaw angles are necessary to counter fluctuations in disturbances. The RMSe values for the collective blade pitch angle and nacelle yaw angle for the H_∞ controller were 0.948 and 0.715 deg. The same values for the LQI controller were 0.380 and 0.275 deg. The consequence of more actuator usage is that the lifetime of actuator mechanisms are reduced. The trade-off that design engineers will have to consider when implementing a controller is therefore reduced fatigue damage caused by lower platform angular velocities, in exchange for reduced actuator usage. A summary

Table 5.1: Value of different specs for the comparison simulation of the H_∞ and LQI controllers. The RMSe value was calculated based on the mean value of each signal

	Maximum overshoot		Mean value		RMSe	
	H_∞	LQI	H_∞	LQI	H_∞	LQI
x_p [m]	13.081	13.065	8.374	7.992	0.669	0.641
y_p [m]	13.436	12.582	8.375	8.054	0.485	0.397
ω_g [deg/s]	110.584	106.966	104.409	101.382	1.670	1.694
$\dot{\theta}_x$ [deg/s]	0.463	0.524	$7.124e^{-5}$	$1.640e^{-4}$	0.066	0.110
$\dot{\theta}_y$ [deg/s]	0.913	0.943	-0.0011	-0.0011	0.245	0.241
β [deg]	-1.957	-4.684	-7.731	-7.3268	0.9475	0.3795
γ [deg]	38.620	37.626	35.721	36.427	0.7151	0.2751
τ_g [N·m]	$3.271e^4$	$3.491e^4$	$3.044e^4$	$3.135e^4$	487.876	536.174

of relevant simulation outputs for the two controllers is listed in Table 5.1.

5.3 Trajectory Tracking

The simulations presented in this section concerned only the H_∞ controller and involved relocating the floating turbine between four points, with each trajectory requiring a different target power output. All selected points lay within the wind turbine's movable range as defined in Section 3.3. The aim of these simulations was to subject the H_∞ controller to a realistic test in which a wind farm controller may assign varying position and power output set-points over time. The turbine trajectory was defined through four points; the initial turbine location O_i, and three remaining locations A, B and C as shown in Figure 5.8. The wind and wave profiles used for this simulation were the same as those used in Section 5.1. The initial turbine position O_i was located at $(11,0)$ m and the target power output at this point was 5 MW. Point A was located at $(8,8)$ m and this position target was activated at time $t = 0$ s. While traveling to point A, the target power output was 3 MW. Point B was located at $(7,0)$ m and this position target was activated at time $t = 300$ s. While traveling to point B, the target power output was 2 MW. Finally, point C was located at $(-5,10)$ m and this position target was activated at time $t = 600$ s. While traveling to point C, the target power output was 4 MW.

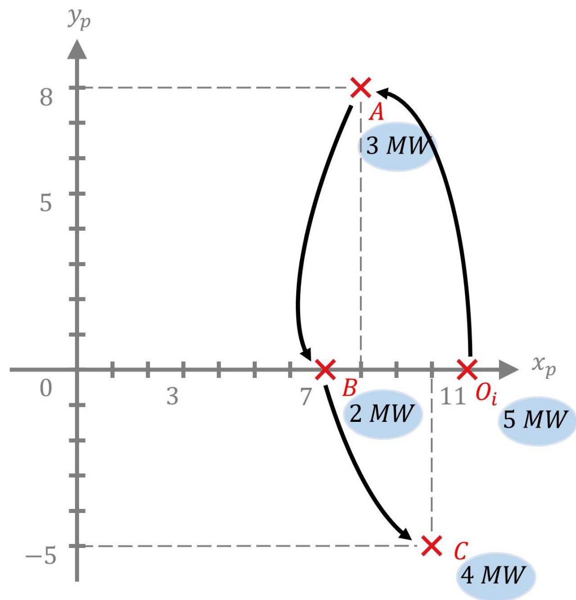

Figure 5.8: OABC trajectory, a black arrow represents the direction from one point to another. Each point shows its corresponding power output marked in blue

The time-domain surge, sway, and power output responses of the closed-loop system are plotted in Figure 5.9. In the case of platform surge, approximately 150 s were required after each new set-point activation for the surge fluctuations to reach their mean values. The required time in the sway direction was approximately 100 s for reaching the final two set-points; this duration was closer to 200 s for the first set-point. RMSe values for the platform surge (calculated relative to the set-points) for the three trajectories were 1.678, 1.119, and 1.095 m in chronological order; as percentages of the set-points, these values were 20.98, 15.99, 10.95 %. These fluctuations in platform surge were unavoidable given that the wind speed in surge direction varied by ± 5 m/s, which was a 27.78 % variation relative to the mean wind speed of 18 m/s.

RMSe values for the platform sway (calculated relative to the set-points) for the three trajectories were 2.654, 2.9251, and 1.961 m in chronological order; as percentages of the set-points, these values were 33.18 %, indeterminable, and 39.22 %. These values are larger than they were in the case of platform surge. One

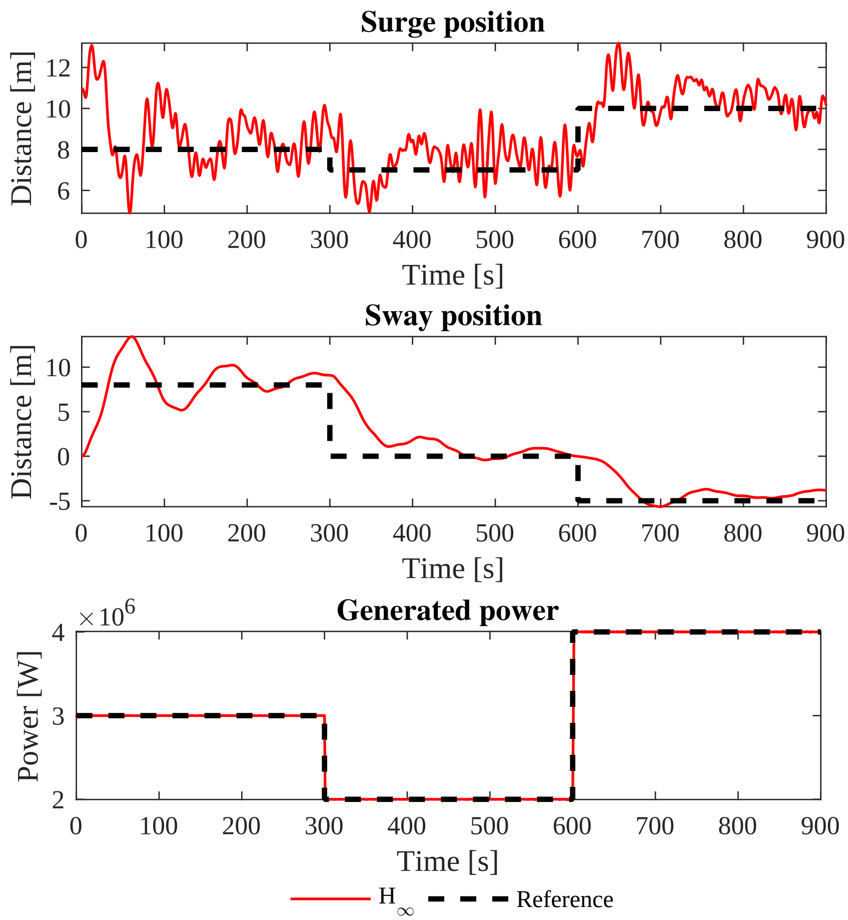

Figure 5.9: Wind turbine surge, sway and power output obtained using the H_∞ controller while following the OABC trajectory. Parameters for the H_∞ controller are listed in Appendix A.2

possible reason is that turbine motion in the sway direction was slower due to a weaker aerodynamic force - the projected rotor area in the crosswind direction is smaller relative to that in the predominant wind direction - which extended the number of time samples over which a large position error persisted. Finally, power output was tracked successfully with RMSe values (calculated relative to the power set-points) as a percentage of the power set-points were equal to 0.022, 0.14, and 0.21 %, in chronological order.

The control inputs calculated for this simulation are presented in Figure 5.10. This information is included for completeness, since a detailed discussion on the progression of the control inputs signals was provided in Section 5.2. One interesting item worth discussing is the spike in the collective blade pitch angle which occurs at $t = 600$ s. At this time, the power output set-point doubles from 2 to 4 MW. In order to increase the power output, the blade pitch angle rotates from a stall position (*i.e.* negative value) toward zero. This action increases the aerodynamic torque acting on the turbine rotor and, when carried out in conjunction

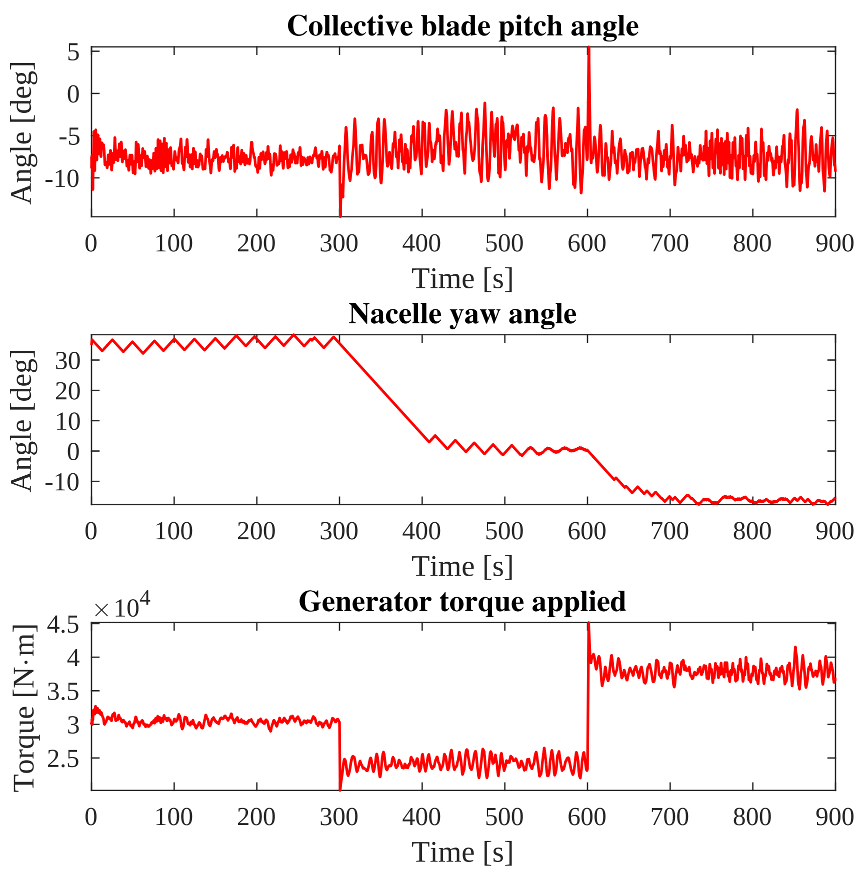

Figure 5.10: Wind turbine control inputs obtained using the H_∞ controller while following the OABC trajectory. Parameters for the H_∞ controller are listed in Appendix A.2

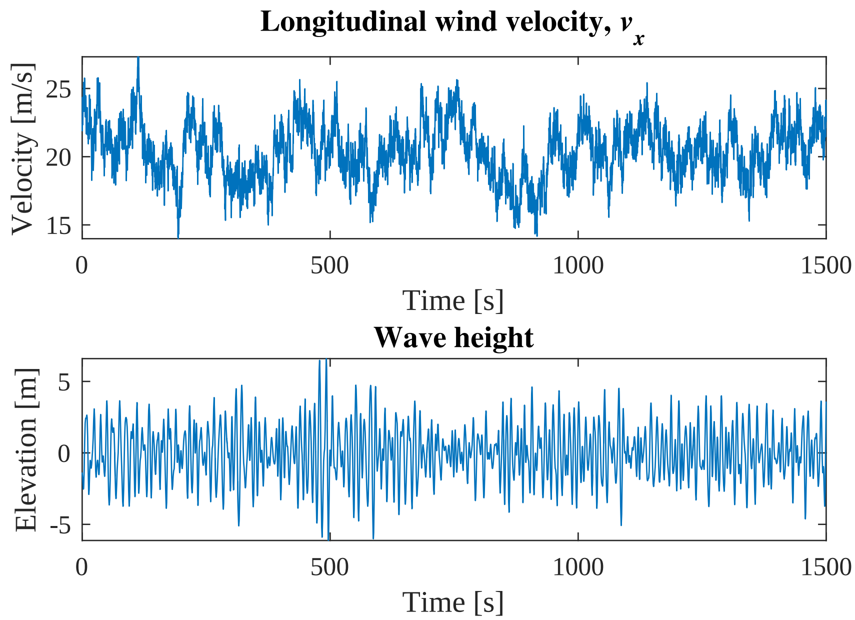

Figure 5.11: For this simulation task, the mean wind and the wave elevation were increased

with an increase in the generator torque, raises the power output. The blade pitch angle actually exceeds zero and approaches 5 deg due to the large initial error in the power output.

5.4 Robustness for Increased Disturbances

The following simulations compare the proposed H_∞ controller to an existing LQI controller with both controllers being subject to increased wind and wave disturbances relative to those simulated in Section 5.2 and Section 5.3. The mean wind speed in the predominant wind direction was increased from 18 to 20 m/s, while the maximum wave elevation was increased from 5 to 8 m. The new disturbance data are plotted in Figure 5.11. Initial conditions and target conditions were the same as those used in Section 5.2; namely, the initial position was (11 m, 0 m), the target position was (8 m, 8 m), and the target power production was 3 MW. The objective of the current section is to evaluate the robustness of both controllers to increased disturbance intensities.

The resulting time-domain angular motion responses of the platform are plotted in Figure 5.12. As before, the H_∞ controller outperforms the LQI when concerned with minimizing the roll angular velocity of the platform. Platform roll velocity RMSe values were 0.115 and 0.136 deg/s for the H_∞ and LQI controllers; the H_∞ controller therefore reduced the roll velocity RMSe by 15.44 %. This value is reduced compared to the 40 % RMSe reduction calculated at lower disturbance intensities in Section 5.2. The H_∞ controller is less effective compared to previous simulations due primarily to the increase in the maximum wave elevation disturbance. As a result, the buoyant forces acting on the platform cylinders are sufficiently large to the point where changes in the blade pitch and yaw angles cannot mitigate fluctuations in the platform roll moment. For example, as the platform roll velocity increases due to the presence of a large wave, the turbine nacelle may yaw to counter the generated rolling moment; however, the more the nacelle yaws in any direction, the smaller the aerodynamic force acting on the rotor becomes. It is therefore clear that there exists a feasible limit on disturbances, particularly wave relate disturbances, beyond which the controller objective of angular motion minimization will be ineffective. As in the previous simulation, the pitch angular velocity RMSe values were the same for both controllers at approximately 0.35 deg/s.

The control signals for the high disturbance simulations are plotted in Figure 5.13. As before, the greater effectiveness of the H_∞ controller in minimizing roll angular motion came at the cost of increased actuator usage. Collective blade pitch angle RMSe values (calculated relative to the mean) were 1.222 and 0.403 deg for the H_∞ and LQI controllers, respectively. Similarly, nacelle yaw angle RMSe values (calculated relative to the mean) were 1.197 and 0.372 deg for these controllers, respectively. In the simulation from Section 5.2, the RMSe values for the collective blade pitch angle and nacelle yaw angle for the H_∞ controller were 0.948 and 0.715 deg; these values have now increased to 1.222 and 1.197 deg. This outcome is not surprising since greater actuator usage is necessary to counter stronger disturbance fluctuations. Concerning the generator torque, the H_∞ controller outperformed the LQI controller in minimizing torque fluctuations. The RMSe values (calculated relative to mean values) were 822.47 and 552.15 N·m; as

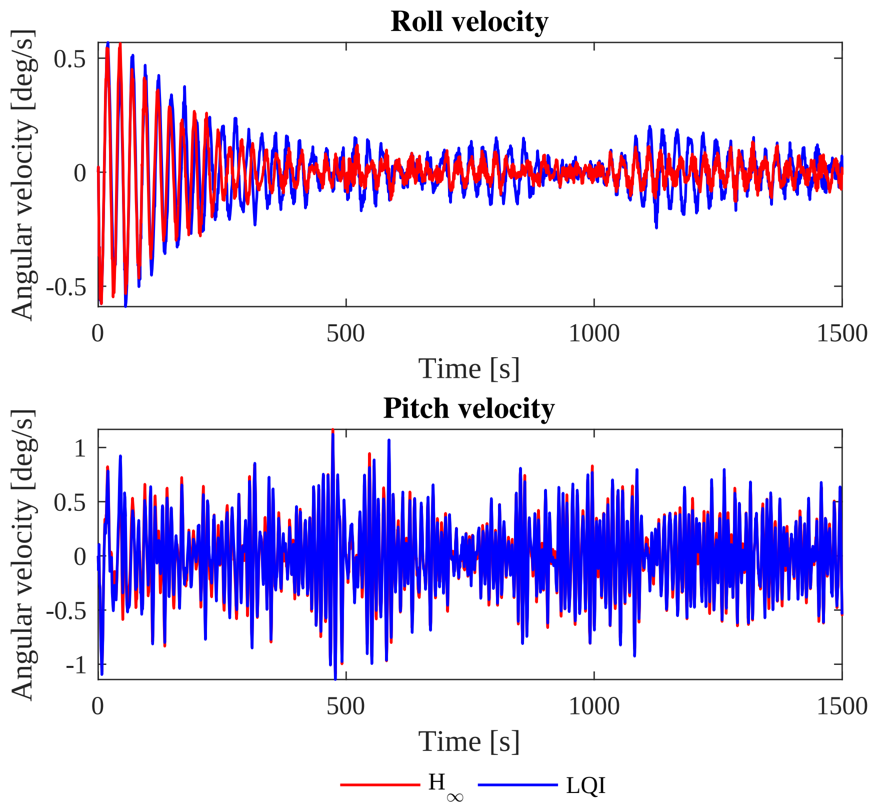

Figure 5.12: Comparison of wind turbine roll and pitch velocities obtained using the H_∞ and LQI controllers under increased disturbance levels. Tuned parameters for the H_∞ and LQI controllers are listed in Appendix A.3

percentages of the respective mean values, these values are 0.026 and 0.017 %.

Another interesting observation is the spike in collective blade pitch angle and generator torque signals corresponding to the LQI controller within the first 50 s of the simulation. This behavior was nonexistent in the control signals corresponding to H_∞ controller, since the H_∞ controller was designed to reject disturbances more effectively. The inability of the LQI controller to reject disturbances as well caused the generator speed to drop at the start of the simulation due to the combined effects of wind and wave disturbances. Specifically, observing the generator speed progression in Figure 5.14, the generator speed fell from 101.9 deg/s to a minimum value of 70.79 deg/s with the trough occurring at a simulation time of $t = 33.95$

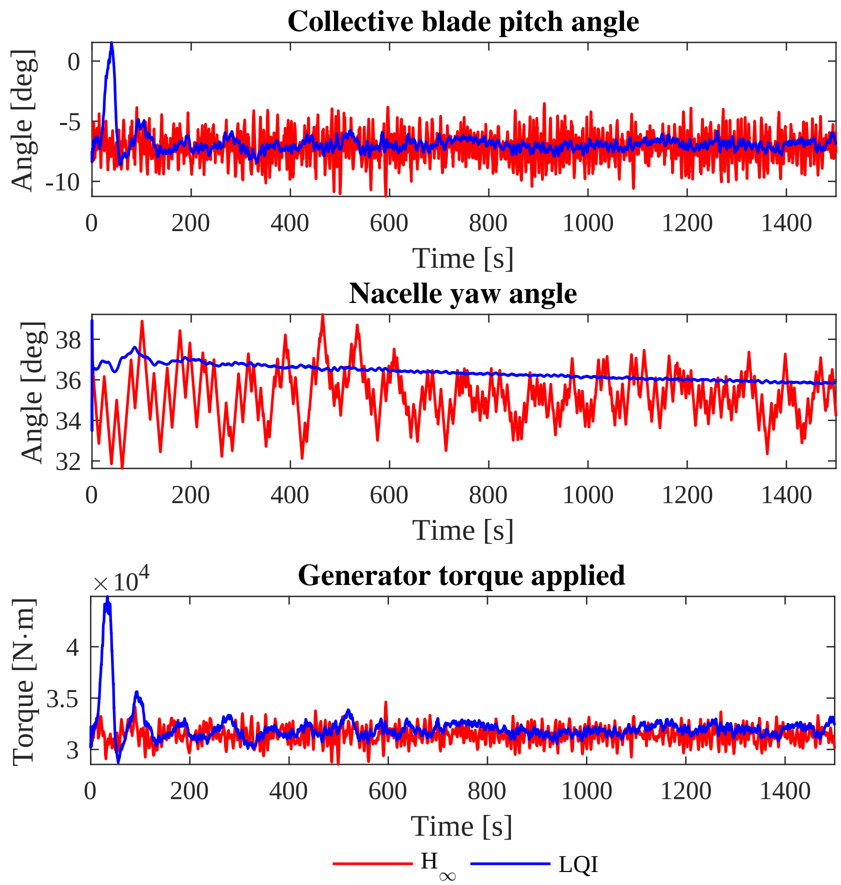

Figure 5.13: Comparison of wind turbine control inputs obtained using the H_∞ and LQI controllers under increased disturbance levels . Tuned parameters for the H_∞ and LQI controllers are listed in Appendix A.3

s. In response, the collective blade pitch angle rose from -7.5 deg to a maximum 1.52 deg with the peak occurring at a simulation time of $t = 39.48$ s. This rise in the collective blade pitch occurred in order to increase the aerodynamic torque applied to the turbine rotor, which in turn increased the generator speed to the appropriate level. A summary of relevant simulation outputs for the two controllers is listed in Table 5.2.

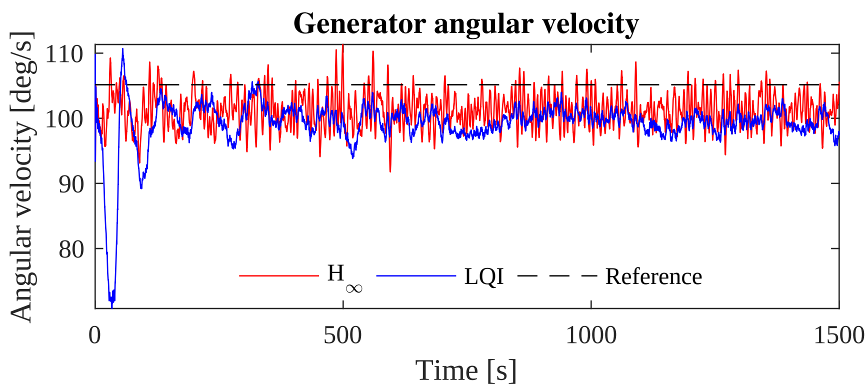

Figure 5.14: Comparison of generator shaft angular speed obtained using the H_∞ and LQI controllers under increased disturbance levels. Tuned parameters for the H_∞ and LQI controllers are listed in Appendix A.3

Table 5.2: Value of different specs for the comparison simulation of the H_∞ and LQI controllers under increased disturbance levels. The RMSe value was calculated based on the mean value of each signal

	Maximum overshoot		Mean value		RMSe	
	H_∞	LQI	H_∞	LQI	H_∞	LQI
x_p [m]	15.426	15.342	8.233	7.998	0.989	0.973
y_p [m]	13.713	11.349	8.246	8.169	0.554	0.381
ω_g [deg/s]	111.329	110.708	101.1976	99.2049	2.6582	3.8260
$\dot{\theta}_x$ [deg/s]	0.564	0.568	-3.30e^{-4}	-3.472e^{-4}	0.115	0.136
$\dot{\theta}_y$ [deg/s]	1.167	1.122	-0.0013	-0.0015	0.35	0.35
β [deg]	-3.517	1.548	-7.163	-6.8627	1.2223	0.9349
γ [deg]	39.226	38.932	35.239	36.371	1.196	0.371
τ_g [N·m]	3.463e^4	4.489e^4	3142.5	3209.2	822.4738	1517.4

Chapter 6

Conclusions

6.1 Summary

The aim of this dissertation was to design a robust H_∞ controller for regulating the position and power output of a floating offshore wind turbine while minimizing its angular motion. An H_∞ controller was employed due to its improved capacity for rejecting disturbances relative to other optimal control systems. This improved capacity stems from the fact that disturbance information matrices are considered in the H_∞ controller design process. The floating wind turbine for which the controller was designed is the NREL baseline 5 MW turbine on a semi-submersible platform.

For controller design, a previously developed nonlinear control-oriented model was utilized. This model was first linearized at an operating point corresponding to the controller targets, then the linearized state-space matrices were used in conjunction with standard H_∞ control system design methods. For controller validation, NREL's FAST software was used. This tool is widely used for wind turbine controller validation due its accuracy in modeling rotor aerodynamics, platform hydrodynamics, mooring line dynamics, and multi-body flexible dynamics.

Simulations were conducted that compared the designed H_∞ controller to a previously designed LQI controller. It was observed that the H_∞ controller successfully tracked position and power output target while reducing platform roll angular motion RMSe values by 40 % under low disturbances (*i.e.* wind speed of 18 m/s and maximum wave height of 5 m) and by 15.5 % under high disturbances (*i.e.* wind speed of 20 m/s and maximum wave height of 8 m) relative to the LQI controller. The H_∞ controller also prevented spikes in the control inputs that were observed when using the LQI controller. These control signal spikes were generated in response to large state value fluctuations that were caused by the LQI controller's relative ineffectiveness in rejecting disturbances.

These improvements in wind turbine platform motion regulation came at the cost of additional actuator usage. Under low disturbances, collective blade pitch angle and nacelle yaw angles RMSe values for the H_∞ controller were approximately 2.5 times larger than those for the LQI controller. Under high disturbance settings, these RMSe values were 3.0 times larger. These numbers indicate that, on average, the magnitudes of actuator fluctuations for the H_∞ controller were 2.5 to 3.0 times larger. Design engineers will therefore have to weigh the effects of excessive actuator mechanism usage over the fatigue damage caused by excessive platform motion. Performing such an analysis requires detailed information regarding the lifetimes of the specific actuators and wind turbine materials employed.

The main contribution from this work was designing an H_∞ controller that regulate the target position and power output of a floating offshore wind turbine, while minimizing angular motion of the turbine platform. To the author's best knowledge, no controller with this specific combination of control objectives has been presented in offshore wind turbine control literature.

6.2 Recommendations

The following recommendations are made for future applications of floating offshore wind turbine position control:

- **The designed multi-objective controller should be designed offline at several operating points for practical implementation.** In this thesis, the proposed H_∞ controller was linearized at each operation point prior to simulation. This approach is impractical in real-world applications due to the high computational costs of optimal controller design. A more feasible approach for implementing this controller would therefore involve offline controller design to obtain optimal controller gain values at each operating point within the movable range of the a turbine, followed by online interpolation to determine the relevant optimal gain value.

- **The proposed multi-objective controller must be validated using experimental techniques.** Although FAST is widely used for controller validation, there is generally a lack of experimental validation within the wind turbine control literature. Constructing an experimental setup for floating offshore wind turbine applications would not only be useful for validating controllers for a single turbine, it would prove especially useful when validating wind farm controllers, since numerically modeling the aerodynamic coupling effect within wind farms is challenging and computationally expensive.

- **A wind farm controller that considers the real-time layout optimization of a floating offshore wind farm must be designed.** As part of continuing the work presented in this thesis, a wind farm controller should be developed with the aim of reducing the wake effect and maximizing power production by means of relocating individual floating wind turbines.

- **The mooring line system of NREL's baseline floating wind turbine must be redesigned in order to expand the movable range.** the wind farm controller mentioned above will only be effective in reducing the wake effect if maximal platform surge and sway values are large enough. Mooring line systems must therefore be redesigned to increase maximum surge and sway values without compromising the stability of the system.

- **Assessing fatigue damage by calculating damage equivalent loading.** The current study only examined platform angular velocity RMSe values as a measure for fatigue damage. A more comprehensive analysis should consider the damage equivalent, which is calculated based on the peak-to-peak load fluctuations and number of load cycles. This information should be used within a cost-benefit analysis that weighs fatigue damage reduction against excessive actuator usage.

Bibliography

[1] J. Jonkman, S. Butterfield, W. Musial, and G. Scott, "Definition of a 5-MW Reference Wind Turbine for Offshore System Development," techreport NREL/TP-500-38060, National Renewable Energy Laboratory (NREL), Golden, Colorado (United States), Feb. 2009.

[2] A. Sharma and S. K. Kar, *Energy Sustainability Through Green Energy*. Springer, 2015.

[3] R. K. Pachauri, M. R. Allen, V. R. Barros, J. Broome, W. Cramer, R. Christ, J. A. Church, L. Clarke, Q. Dahe, P. Dasgupta, *et al.*, *Climate change 2014: synthesis report. Contribution of Working Groups I, II and III to the fifth assessment report of the Intergovernmental Panel on Climate Change*. IPCC, 2014.

[4] T. M. Letcher, *Wind Energy Engineering: A Handbook for Onshore and Offshore Wind Turbines*. London; San Diego, CA: Academic Press, 2017.

[5] J. G. Schepers and S. P. Van der Pijl, "Improved modelling of wake aerodynamics and assessment of new farm control strategies," in *Journal of Physics: Conference Series*, vol. 75, p. 012039, IOP Publishing, 2007.

[6] L. Castro-Santos and V. Diaz-Casas, *Floating Offshore Wind Farms*. Springer, 2016.

[7] L. Y. Pao and K. E. Johnson, "Control of wind turbines," *IEEE Control Systems*, vol. 31, no. 2, pp. 44–62, 2011.

[8] M. Karimirad and T. Moan, "Feasibility of the application of a spar-type wind turbine at a moderate water depth," *Energy Procedia*, vol. 24, pp. 340–350, 2012.

[9] S. Butterfield, W. Musial, J. Jonkman, and P. Sclavounos, "Engineering challenges for floating offshore wind turbines," Tech. Rep. NREL/CP-500-38776, National Renewable Energy Laboratory (NREL), Golden, Colorado (United States), Sept. 2007.

[10] A. Myhr, T. A. Nygaard, *et al.*, "Load reductions and optimizations on tension-leg-buoy offshore wind turbine platforms," in *The Twenty-second International Offshore and Polar Engineering Conference*, International Society of Offshore and Polar Engineers, 2012.

[11] J. Zhao, L. Zhang, and H. Wu, "Motion performance and mooring system of a floating offshore wind turbine," *Journal of Marine Science and Application*, vol. 11, no. 3, pp. 328–334, 2012.

[12] D. Roddier, C. Cermelli, A. Aubault, and A. Weinstein, "WindFloat: a floating foundation for offshore wind turbines," *Journal of Renewable and Sustainable Energy*, vol. 2, no. 3, p. 033104, 2010.

[13] F. Koch, M. Gresch, F. Shewarega, I. Erlich, and U. Bachmann, "Consideration of wind farm wake effect in power system dynamic simulation," in *Power Tech, 2005 IEEE Russia*, pp. 1–7, IEEE, 2005.

[14] K. E. Johnson, "Adaptive torque control of variable speed wind turbines," techreport NREL/TP-500-36265, National Renewable Energy Laboratory (NREL), Golden, Colorado (United States), Aug. 2004.

[15] R. J. Barthelmie, O. Rathmann, S. T. Frandsen, K. S. Hansen, E. Politis, J. Prospathopoulos, K. Rados, D. Cabezon, W. Schlez, J. Phillips, *et al.*, "Modelling and measurements of wakes in large wind farms," in *Journal of Physics: Conference Series*, vol. 75, IOP Publishing, 2007.

[16] K. E. Johnson and N. Thomas, "Wind farm control: Addressing the aerodynamic interaction among wind turbines," in *American Control Conference (ACC), 2009*, pp. 2104–2109, IEEE, June 2009.

[17] T. Knudsen, T. Bak, and M. Svenstrup, "Survey of wind farm control - power and fatigue optimization," *Wind Energy*, vol. 18, no. 8, pp. 1333–1351, 2015.

[18] Á. Jiménez, A. Crespo, and E. Migoya, "Application of a LES technique to characterize the wake deflection of a wind turbine in yaw," *Wind Energy*, vol. 13, no. 6, pp. 559–572, 2009.

[19] J. W. Wagenaar, L. Machielse, and J. Schepers, "Controlling wind in ECN's scaled wind farm," *Proc. Europe Premier Wind Energy Event*, pp. 685–694, 2012.

[20] M. T. van Dijk, J.-W. van Wingerden, T. Ashuri, and Y. Li, "Wind farm multi-objective wake redirection for optimizing power production and loads," *Energy*, vol. 121, pp. 561–569, 2017.

[21] S. Guntur, N. Troldborg, and M. Gaunaa, "Application of engineering models to predict wake deflection due to a tilted wind turbine," in *EWEA 2012-European Wind Energy Conference & Exhibition*, European Wind Energy Association (EWEA), 2012.

[22] P. A. Fleming, P. M. O. Gebraad, S. Lee, J.-W. van Wingerden, K. Johnson, M. Churchfield, J. Michalakes, P. Spalart, and P. Moriarty, "Evaluating techniques for redirecting turbine wakes using SOWFA," *Renewable Energy*, vol. 70, pp. 211–218, 2014.

[23] P. Fleming, P. M. O. Gebraad, S. Lee, J.-W. Wingerden, K. Johnson, M. Churchfield, J. Michalakes, P. Spalart, and P. Moriarty, "Simulation comparison of wake mitigation control strategies for a two-turbine case," *Wind Energy*, vol. 18, no. 12, pp. 2135–2143, 2015.

[24] A. J. Sørensen, "A survey of dynamic positioning control systems," *Annual Reviews in Control*, vol. 35, no. 1, pp. 123–136, 2011.

[25] S. F. Rodrigues, R. Teixeira Pinto, M. Soleimanzadeh, P. Bosman, and P. Bauer, "Wake losses optimization of offshore wind farms with moveable floating wind turbines," *Energy Conversion and Management*, vol. 89, pp. 933–941, 2015.

[26] Y. Li and Z. Wu, "Stabilization of floating offshore wind turbines by artificial muscle based active mooring line force control," in *American Control Conference (ACC), 2016*, pp. 2277–2282, July 2016.

[27] C. Han, J. R. Homer, and R. Nagamune, "Movable range and position control of an offshore wind turbine with a semi-submersible floating platform," in *American Control Conference (ACC), 2017*, pp. 1389–1394, IEEE, May 2017.

[28] C. Han, "Position control of a floating offshore wind turbine system using aerodynamic force," Master's thesis, The University of British Columbia, 2017.

[29] M. A. Lackner and M. A. Rotea, "Passive structural control of offshore wind turbines," *Wind Energy*, vol. 14, no. 3, pp. 373–388, 2010.

[30] S. Colwell and B. Basu, "Tuned liquid column dampers in offshore wind turbines for structural control," *Engineering Structures*, vol. 31, no. 2, pp. 358–368, 2009.

[31] A. Di Matteo, F. Lo Iacono, G. Navarra, and A. Pirrotta, "The Control Performance of TLCD and TMD: Experimental Investigation," in *5th European Conference on Structural Control*, pp. 18–20, 2012.

[32] S. Christiansen, T. Knudsen, and T. Bak, "Extended onshore control of a floating wind turbine with wave disturbance reduction," *Journal of Physics: Conference Series*, vol. 555, no. 1, p. 012018, 2014.

[33] S. Christiansen, S. M. Tabatabaeipour, T. Bak, and T. Knudsen, "Wave disturbance reduction of a floating wind turbine using a reference model-based predictive control," in *American Control Conference (ACC), 2013*, pp. 2214–2219, June 2013.

[34] M. Geyler and P. Caselitz, "Robust multivariable pitch control design for load reduction on large wind turbines," *Journal of Solar Energy Engineering*, vol. 130, no. 3, p. 031014, 2008.

[35] P. A. Fleming, J.-W. van Wingerden, A. K. Scholbrock, G. van der Veen, and A. D. Wright, “Field testing a wind turbine drivetrain/tower damper using advanced design and validation techniques,” in *American Control Conference (ACC), 2013*, pp. 2227–2234, IEEE, 2013.

[36] E. de Vries, “Multibrid: a new offshore wind turbine contender,” *Renewable Energy World*, vol. 7, pp. 52–65, 2004.

[37] D. J. Malcolm and A. C. Hansen, “WindPACT Turbine Rotor Design Study: June 2000–June 2002 (Revised),” Tech. Rep. NREL/SR-500-32495, National Renewable Energy Laboratory (NREL), Golden, Colorado (United States), Apr. 2006.

[38] F. Goezinne, “Terms of reference DOWEC,” *NEG-Micon. Bunnik*, 2001.

[39] P. W. Carlin, A. S. Laxson, and E. B. Muljadi, “The history and state of the art of variable-speed wind turbine technology,” *Wind Energy*, vol. 6, no. 2, pp. 129–159, 2003.

[40] A. Robertson, J. Jonkman, M. Masciola, H. Song, A. Goupee, A. Coulling, and C. Luan, “Definition of the Semisubmersible Floating System for Phase II of OC4,” Tech. Rep. NREL/TP-5000-60601, National Renewable Energy Laboratory, Golden, Colorado (United States), Sept. 2014.

[41] H. Namik and K. Stol, “Performance analysis of individual blade pitch control of offshore wind turbines on two floating platforms,” *Mechatronics*, vol. 21, no. 4, pp. 691–703, 2011.

[42] D. C. Quarton, “An international design standard for offshore wind turbines: IEC 61400-3,” *Garrad Hassan and Partners Ltd*, 2005.

[43] J. M. Jonkman and M. L. Buhl Jr, “FAST User’s Guide-Updated August 2005,” Tech. Rep. NREL/TP-500-38230, National Renewable Energy Laboratory (NREL), Golden, Colorado (United States), Oct. 2005.

[44] A. Manjock, “Evaluation report: Design codes FAST and ADAMS for load calculations of onshore wind turbines,” *Germanischer Lloyd WindEnergie GmbH, Rept*, vol. 72042, 2005.

[45] J. R. Homer, "Physics-Based Control-Oriented Modelling for Floating Offshore Wind Turbines," Master's thesis, The University of British Columbia, 2015.

[46] H. Baruh, *Analytical dynamics*. WCB/McGraw-Hill Boston, 1999.

[47] J. M. Jonkman, "Dynamics Modeling and Loads Analysis of an Offshore Floating Wind Turbine," Tech. Rep. NREL/TP-500-41958, National Renewable Energy Laboratory (NREL), Golden, Colorado (United States), Nov. 2007.

[48] P. J. Moriarty and A. C. Hansen, *AeroDyn theory manual*. National Renewable Energy Laboratory Golden, CO, 2005.

[49] J. M. Jonkman, A. Robertson, and G. J. Hayman, "HydroDyn user's guide and theory manual," *National Renewable Energy Laboratory*, 2014.

[50] M. Hall, "MoorDyn - user's guide," *Department of Mechanical Engineering, University of Maine*, 2015.

[51] J. R. Homer and R. Nagamune, "Physics-based 3-D control-oriented modeling of floating wind turbines," *IEEE Transactions on Control Systems Technology*, vol. 26, no. 1, pp. 14–26, 2018.

[52] G.-R. Duan and H.-H. Yu, *LMIs in Control Systems: Analysis, Design and Applications*. CRC Press, 2013.

[53] P. Gahinet, A. Nemirovski, A. J. Laub, and M. Chilali, *The LMI Control Toolbox. For Use with MATLAB*. The MathWorks, Inc., 1995.

[54] B. J. Jonkman, "TurbSim User's Guide: Version 1.50," Tech. Rep. NREL/TP-500-46198, National Renewable Energy Laboratory (NREL), Golden, Colorado (United States), Sept. 2009.

Appendix A

Controller values

A.1 Values Used to the Regulation Comparison H_∞ vs LQI task

The values employed for the comparison of the H_∞ controller and the LQI controller are set in the following section. Firstly, the initial conditions of the states and the control inputs

$$\vec{x}_0 = \begin{bmatrix} 8.0000 \\ 8.0000 \\ -9.9478 \\ -0.0424 \\ 0.0568 \\ 0.0003 \\ 0.0000 \\ 0.0000 \\ 0.0000 \\ 0.0000 \\ 0.0000 \\ 0.0000 \\ 1.0840 \\ 105.1527 \\ 0.0034 \end{bmatrix}, \quad \vec{u}_0 = \begin{bmatrix} -0.1455 \\ 30222.3857 \\ 0.6380 \end{bmatrix},$$

and the weight matrices $\mathbf{W}_\phi$ and $\mathbf{W}_{u'}$

$$\mathbf{W}_\phi = \begin{bmatrix} 0.2 & 0 & 0 & 0 & 0 \\ 0 & 0.2 & 0 & 0 & 0 \\ 0 & 0 & 70 & 0 & 0 \\ 0 & 0 & 0 & 908 & 0 \\ 0 & 0 & 0 & 0 & 608 \end{bmatrix}, \quad \mathbf{W}_{u'} = \begin{bmatrix} 135 & 0 \\ 0 & 30 \end{bmatrix}.$$

The state-feedback H_∞ controller transpose gain calculated

$$\mathbf{K}_\infty^T = \begin{bmatrix} 0.0007 & -0.0032 \\ 0.0012 & 0.0006 \\ 0.0006 & -0.0013 \\ -0.7754 & 1.8532 \\ 0.4136 & 1.1222 \\ -0.0368 & 0.5806 \\ -0.0519 & 0.1619 \\ -0.0515 & -0.1434 \\ -0.0074 & -0.0038 \\ 12.1777 & 33.8418 \\ -6.7712 & 26.3235 \\ 4.6385 & -6.5654 \\ -1.2309 & 0.5298 \\ -0.0018 & 0.0008 \\ 0.0536 & -0.0242 \end{bmatrix}.$$

For the LQI controller, the weights $\mathbf{Q}$ and $\mathbf{R}$ employed are

$$\mathbf{Q} = \begin{bmatrix} \mathbf{0}_{12\times12} & \mathbf{0}_{12\times4} & \\ & 1 & \mathbf{0}_{1\times3} \\ \mathbf{0}_{4\times12} & \mathbf{0}_{2\times4} & \\ & \mathbf{0}_{2\times2} & \mathbf{I}_2 \end{bmatrix}, \quad \mathbf{R} = \begin{bmatrix} 4e^6 & 0 & 0 \\ 0 & 5e^6 & 0 \\ 0 & 0 & 1e^7 \end{bmatrix}.$$

The transpose gain values without including the integrator part is

$$\mathbf{K}_{LQI}^{T} = \begin{bmatrix} 0.0012 & -0.0002 & 0.0002 \\ 0.0005 & -0.0000 & 0.0001 \\ -0.0000 & 0.0000 & -0.0000 \\ -0.0192 & 0.0019 & -0.0038 \\ 0.0204 & -0.0021 & 0.0041 \\ -0.0326 & 0.0016 & -0.0065 \\ 0.1317 & -0.0415 & 0.0263 \\ 0.0546 & 0.0310 & 0.0109 \\ -0.0005 & 0.0000 & -0.0001 \\ -0.0034 & 0.0123 & -0.0007 \\ -0.1533 & 0.0325 & -0.0307 \\ -0.5768 & -0.1177 & -0.1154 \\ 0.0452 & -0.0044 & 0.0090 \\ 0.0001 & -0.0000 & 0.0000 \\ 0.0035 & -0.0003 & 0.0007 \end{bmatrix},$$

and the integrator gain is

$$\mathbf{K}_{I} = \begin{bmatrix} -0.0004 & -0.0001 \\ 0.0002 & -0.0001 \\ -0.0001 & -0.0000 \end{bmatrix}.$$

A.2 Values Used to the Trajectory Task

The following table contains the information regarding the trajectory task.

Table A.1: A list of the H_∞ controller gains and initial conditions used for the trajectory described as $\{(x_p, y_p), P_{tar}[\text{MW}]\}$

	$(8,8),2$		$(7,0),3$		$(10,-5),4$	
$\mathbf{K}_\infty^T$	0.0007	-0.0032	0.0008	0.0000	0.0014	-0.0012
	0.0012	0.0006	-0.0000	0.0012	-0.0002	0.0045
	0.0006	-0.0013	0.0001	-0.0000	-0.0005	0.0012
	-0.7754	1.8530	-0.0003	2.0367	-0.1058	3.5471
	0.4137	1.1219	0.0685	-0.0015	0.2180	-0.5409
	-0.0363	0.5793	0.0007	-0.0193	-0.0668	-0.2110
	-0.0518	0.1618	-0.0736	0.0000	-0.0785	0.0398
	-0.0514	-0.1433	0.0000	-0.2354	0.0352	-0.3447
	-0.0074	-0.0038	0.0087	-0.0000	-0.0064	0.0062
	12.1692	33.8463	-0.0049	52.8476	-6.0228	58.6173
	-6.7664	26.3210	-13.9779	-0.0062	-12.9130	-7.6285
	4.6263	-6.5494	-0.0071	2.9906	-9.6344	60.0839
	-1.2300	0.5293	-1.4252	-0.0000	-1.2570	0.3430
	-0.0018	0.0008	-0.0020	-0.0000	-0.0018	0.0005
	0.0536	-0.0241	0.0920	0.0000	0.0838	-0.0294
x_0	8.0000		7.0000		10.0000	
	8.0000		0.0000		-5.0000	
	-9.9478		-9.9274		-9.9579	
	-0.0424		0.0000		0.0245	
	0.0568		0.0524		0.0792	
	0.0003		-0.0000		-0.0004	
	0.0000		0.0000		0.0000	
	0.0000		0.0000		0.0000	
	0.0000		0.0000		0.0000	
	0.0000		0.0000		0.0000	
	0.0000		0.0000		0.0000	
	0.0000		0.0000		0.0000	
	1.0860		0.8808		1.1645	
	105.3426		85.4363		112.9542	
	0.0022		0.0042		0.0042	
u_0	-0.1741		-0.0663		-0.1389	
	20111.9495		37196.9076		37513.3135	
	0.6380		-0.0000		-0.2938	

A.3 Values Used for the Increased Disturbance task

The values employed for the comparison of the H_∞ controller and the LQI controller are set in the following section. Firstly, the initial conditions of the states and the control inputs

$$\vec{x}_0 = \begin{bmatrix} 8.0000 \\ 8.0000 \\ -9.9478 \\ -0.0424 \\ 0.0568 \\ 0.0003 \\ 0.0000 \\ 0.0000 \\ 0.0000 \\ 0.0000 \\ 0.0000 \\ 0.0000 \\ 1.071 \\ 103.891 \\ 0.0034 \end{bmatrix}, \quad \vec{u}_0 = \begin{bmatrix} -0.1410 \\ 30589.309 \\ 0.6380 \end{bmatrix},$$

and the weight matrices W_ϕ and $W_{u'}$

$$W_\phi = \begin{bmatrix} 0.4 & 0 & 0 & 0 & 0 \\ 0 & 0.4 & 0 & 0 & 0 \\ 0 & 0 & 120 & 0 & 0 \\ 0 & 0 & 0 & 900 & 0 \\ 0 & 0 & 0 & 0 & 600 \end{bmatrix}, \quad W_{u'} = \begin{bmatrix} 300 & 0 \\ 0 & 30 \end{bmatrix}.$$

The state-feedback H_∞ controller transpose gain calculated

$$
\mathrm{K}_{\infty}^{T} = \begin{bmatrix}
0.0014 & -0.0011 \\
-0.0005 & 0.0024 \\
-0.0015 & -0.0148 \\
0.0123 & 3.2620 \\
0.2502 & 1.5512 \\
-0.3560 & 1.0965 \\
-0.0639 & 0.0506 \\
-0.0201 & -0.5103 \\
0.0099 & 0.0126 \\
3.3660 & 57.2836 \\
-5.2162 & -0.6727 \\
5.5205 & 3.1162 \\
-1.0066 & -3.4723 \\
-0.0015 & -0.0050 \\
0.0523 & 0.2079
\end{bmatrix}.
$$

For the LQI controller, the weights **Q** and **R** employed are

$$
\mathbf{Q} = \begin{bmatrix}
\mathbf{0}_{12\times12} & \mathbf{0}_{12\times4} \\
 & \begin{matrix} 1 & \mathbf{0}_{1\times3} \end{matrix} \\
\mathbf{0}_{4\times12} & \mathbf{0}_{2\times4} \\
 & \begin{matrix} \mathbf{0}_{2\times2} & \mathbf{I}_2 \end{matrix}
\end{bmatrix}, \quad
\mathbf{R} = \begin{bmatrix}
4e^6 & 0 & 0 \\
0 & 5e^6 & 0 \\
0 & 0 & 1e^7
\end{bmatrix}.
$$

The transpose gain values without including the integrator part is

$$
K_{LQI}^{T} = \begin{bmatrix}
0.0021 & -0.0001 & 0.0004 \\
0.0006 & 0.0001 & 0.0001 \\
0.0002 & 0.0000 & 0.0000 \\
0.0154 & 0.0005 & 0.0031 \\
-0.0240 & -0.0006 & -0.0048 \\
-0.0180 & 0.0002 & -0.0036 \\
0.1382 & -0.0293 & 0.0276 \\
0.0551 & 0.0351 & 0.0110 \\
-0.0008 & 0.0000 & -0.0002 \\
-0.0658 & 0.0100 & -0.0132 \\
-0.0195 & 0.0195 & -0.0039 \\
-0.0715 & 0.0721 & -0.0143 \\
0.0390 & -0.0004 & 0.0078 \\
0.0001 & -0.0000 & 0.0000 \\
0.0032 & -0.0000 & 0.0006
\end{bmatrix},
$$

and the integrator gain is

$$
K_{I} = \begin{bmatrix}
-0.0005 & -0.0001 \\
0.0002 & -0.0001 \\
-0.0001 & -0.0000
\end{bmatrix}
$$